Cerebral edema evolution and the role of aquaporin-4 in secondary injury after acute ischemic stroke

dr. Réka Tóth

PhD Thesis

Szeged, 2026

University of Szeged
Albert Szent-Györgyi Medical School
Doctoral School of Experimental and Preventive Medicine

Cerebral edema evolution and the role of aquaporin-4 in secondary injury after acute ischemic stroke

PhD Thesis

dr. Réka Tóth

Supervisor: Dr. Ákos Menyhárt

Szeged, 2026

CONTENTS

PUBLICATIONS RELATED TO THE PHD THESIS

1. Tóth R, Farkas AE, Krizbai IA, Makra P, Bari F, Farkas E and Menyhárt Á.

Astrocyte Ca^{2+} Waves and Subsequent Non-Synchronized Ca^{2+} Oscillations Coincide with Arteriole Diameter Changes in Response to Spreading Depolarization

International Journal of Molecular Sciences 2021 Mar 26;22(7):3442.
doi: 10.3390/ijms22073442. PMID: 33810538; PMCID: PMC8037646.

2. Tóth R, Szabó N, Törteli A, Kovács N, Horváth I, Szigeti K, Máthé D, Kincses TZ, Menyhárt Á, Farkas E.

The paradoxical relationship of sensorimotor deficit and lesion volume in acute ischemic stroke

Journal of Neuropathology & Experimental Neurology 2025 Sep 1;84(9):771-779.
doi: 10.1093/jnen/nlaf046. PMID: 40272944; PMCID: PMC12365491.

3. Tóth R, Törteli A, Szabó M, Kovács N, Horváth I, Farkas A, Frank R, Szigeti K, Bari F, Krizbai IA, Máthé D, Menyhárt Á, Farkas E.

Trifluoperazine reduces infarct size, restores neurovascular coupling and improves early outcomes in experimental acute ischemic stroke

Currently under review at Journal of Cerebral Blood Flow and Metabolism, 2026

ABBREVIATIONS

%HLV: hemispheric lesion volume

%HSE: increase of total hemispheric volume

aCSF: artificial cerebrospinal fluid

ADC: apparent diffusion coefficient

AIS: acute ischemic stroke

AQP4: aquaporin-4

BBB: blood-brain barrier

CaM: calmodulin

CBF: cerebral blood flow

CE: cerebral edema

CNS: central nervous system

CSF: cerebrospinal fluid

DC: direct current

GNS: Garcia Neuroscore Scale

L/R ratio: ratio of left/ right brain hemispheres

LFP: local field potential

LV and **LVc**: lesion volume and edema-corrected lesion volume

LVO: large vessel occlusion

MCA: middle cerebral artery

MCAO: middle cerebral artery occlusion

MRI: magnetic resonance imaging

NVC: neurovascular coupling

NVU: neurovascular unit

OAP: orthogonal array of particles

SD: spreading depolarization

SPECT: Single Photon Emission Computed Tomography

SUV: Standardized uptake value

TFP: trifluoperazine

INTRODUCTION

The etiology of stroke and state-of-the-art treatment options

Sudden hemiplegia, one-sided numbness, facial asymmetry or speech difficulty are classic signs of acute cerebrovascular events that demand immediate medical attention to prevent severe consequences, including death. Stroke affects nearly 94 million people worldwide and remains the second leading cause of death and the third leading cause of death and disability combined. Although 84% of strokes are linked to modifiable risk factors, hypertension, excess weight, poor diet, smoking and low physical activity due to modern lifestyles continue to drive risk. Due to that, between 1990 and 2021, stroke incidence rose by 70%, and related deaths and disability doubled. Today, almost 12 million new cases occur annually, with 7 million resulting in death. Beyond the profound impact on families, global spending on stroke care reaches 890 billion USD each year and is expected to double by 2025[1], underscoring the urgent need for continued stroke research.

Stroke is defined as an acute onset focal neurological deficit with no other explanation than a disturbance in the cerebral circulation[2]. The brain is richly supplied with blood by the carotid and vertebral systems, however, because of the constant high energy demand and the lack of reserves, the abrupt cessation of blood flow in any of the brain arteries can have a devastating effect[3]. Stroke can be divided into two major subtypes depending on the cause: hemorrhagic, which account for approximately 13% of all stroke cases and ischemic being the majority in 87% of patients[4]. In hemorrhagic stroke, rupture of a cerebral blood vessel results in extravasation of blood into the brain parenchyma or the subarachnoid space. Although less frequent than ischemic events, 30-day mortality of cerebral bleeding may approach 50%, underscoring its severity. Primary intracerebral hemorrhage (ICH) most commonly arises from small-vessel pathology, particularly hypertensive microangiopathy or cerebral amyloid angiopathy. Secondary ICH may occur due to structural abnormalities such as vascular malformations or tumors, coagulopathies, or as hemorrhagic transformation of an ischemic infarct[5]. Subarachnoid hemorrhage is of traumatic origin in approximately 15% of cases, whereas the remaining non-traumatic cases—around 85%—are predominantly caused by rupture of an intracranial aneurysm[6, 7].

Because acute ischemic stroke (AIS) accounts for the majority of stroke cases, it remains a major focus of intensive research, including the present study. In the setting of AIS, blood flow to a region of the brain is ceased because of the occlusion of the supplying artery (Fig. 1). There

are several classification systems that categorize the different origins of stroke, but they all distinguish five major subtypes[8-10]. Large-artery atherosclerosis represents the first major subtype, encompassing occlusion at the site of a stenotic plaque or distal embolization from thrombus formation on a ruptured plaque. The second category, cardioembolism, typically an embolus originating from left atrial appendage thrombi in patients with untreated atrial fibrillation dislodges and blocks a cranial vessel. Occlusions of either atherosclerotic or cardioembolic origin affecting the internal carotid artery (ICA), the proximal segments of the posterior, middle, and anterior cerebral arteries (PCA, MCA, and ACA, respectively), as well as the vertebral (VA) or basilar arteries (BA), are classified as large vessel occlusions (LVOs), which account for up to 46% of AIS.[11]. The third subtype comprises small-artery occlusions, often referred to as lacunary stroke. Fourth category describes strokes of other determined, miscellaneous etiologies, such as hematologic disorders, non-atherosclerotic vasculopathies or hypercoagulable states, while the fifth subtype covers cases of undetermined etiology.

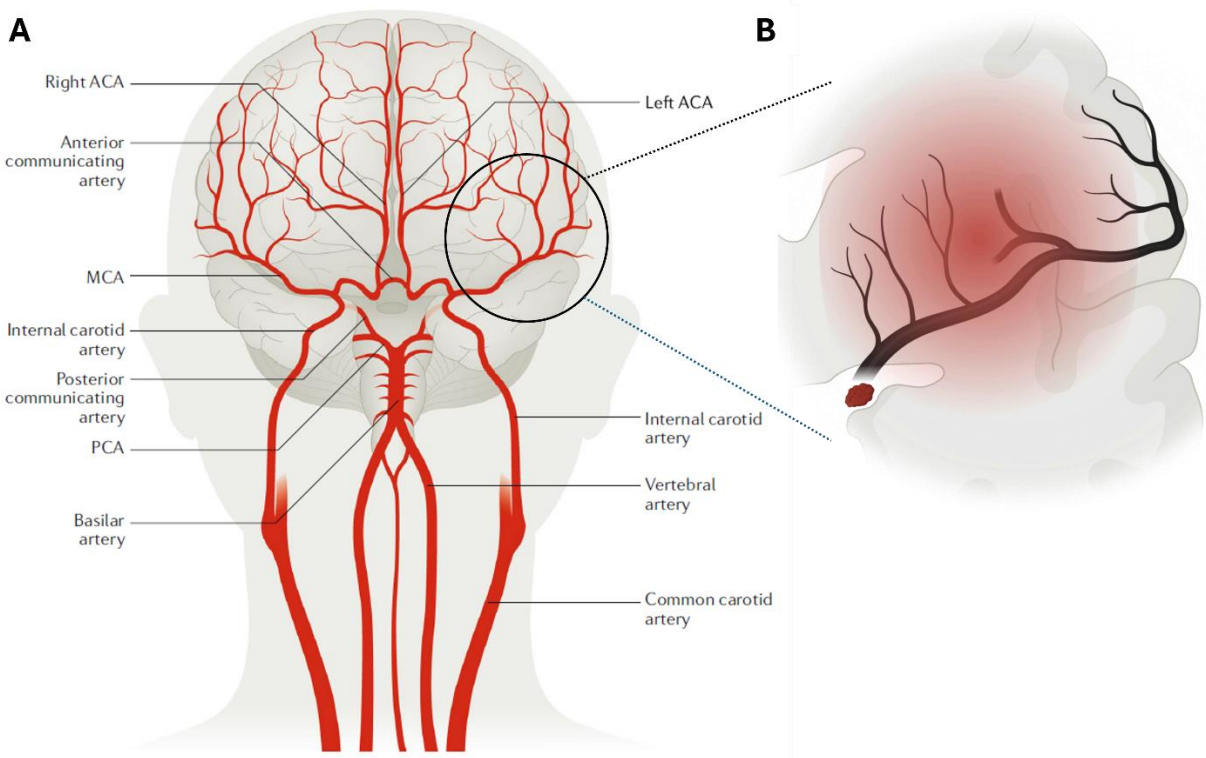

Figure 1. Ischemic stroke is most commonly caused by the occlusion of an extra- or intracranial large vessel. A, Major arteries supplying the brain. **B,** Acute ischemic stroke is caused by the occlusion of a cerebral artery by a thrombus. Cerebral regions with compromised blood flow distal to the occlusion are marked as red area. ACA: anterior cerebral artery, MCA: middle cerebral artery, PCA: posterior cerebral artery.
Figure was adapted and modified from Campbell et al., 2019.

In ischemic brain tissue, the cessation of blood flow results in depletion of oxygen and nutrients essential for neurons and glial cells. This deficiency first causes the loss of Na^+/K^+ ATPase function therefore the loss of ability of the cells to maintain their membrane potential, leading

to cell depolarization, which in turn triggers a series of pathological cascades that eventually lead to cell death. The center of the ischemic injury is called the ischemic core, where the profound decrease in cerebral blood flow (CBF) (<10 ml/100g tissue/min or 10%-25%) leads to irreversible cellular damage[12] (Fig. 2). It has been identified already in the 1970s, that the initial clinical deficit observed in stroke patients is due to a hypoperfused, dynamically changing area around the core region called the penumbra, with perfusion reduced to between 20-40 ml/100g/min (Fig. 2). In this area, cells are electrically silent but viable, and cells in this area can still be rescued by timely restoration of blood supply. Because the penumbra irreversibly evolves into the infarct core with increasing time spent in ischemia, reperfusion of the tissue at risk as soon as possible is essential and represents the aim of all stroke therapies. [13, 14] .

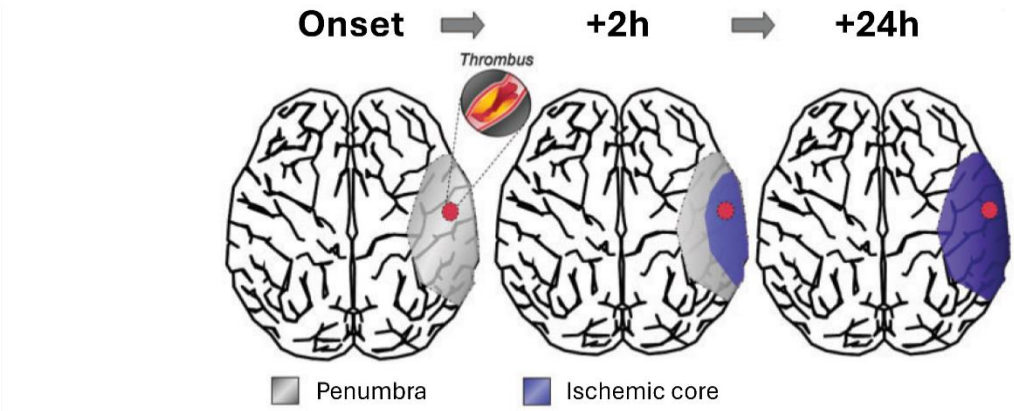

Figure 2. Ischemic core expands over time at the expense of the penumbra. Figure was adapted and modified from Gauberti et al., 2016[15].

Intravenous thrombolysis with tissue plasminogen activator drug alteplase was approved by the Food and Drug Administration (FDA) in the United States for the treatment of ischemic stroke within a time window of 4.5 hours in 1996 and has been in the use ever since. Based on the evidences of the EXTEND trial[16], the time window was extended to 9 hours in 2019 and most recently in March 2025 tenecteplase became FDA approved making it the first approval of a new stroke thrombolytic in nearly 30 years[17]. Following intensive research and multiple clinical trials beginning in the early 2000s, direct clot removal by mechanical thrombectomy within 6 hours of symptom onset became the standard of care in selected LVO cases in 2015[14] (Fig. 3). The DAWN and DEFUSE 3 trials provided evidence that certain patients may benefit from mechanical thrombectomy for up to 24 hours from last known well[18, 19]. Moreover, studies published in the last 3 years demonstrate that even patients with severe symptoms and large infarct cores may achieve better outcomes when treated with thrombectomy, thereby further expanding the pool of candidates for intervention[14, 20-22].

Although reperfusion therapies have advanced substantially, current stroke treatment remains limited. Even after successful recanalization, delayed infarct progression can occur[23], and in some cases reperfusion may exacerbate the injury[24] (Fig. 2&3) or no-reflow may follow the technically successful intervention. Despite extensive investment in stroke research in the past 30 years, none of the over 1000 neuroprotective agents effective in preclinical studies have translated into clinical benefit, highlighting a persistent "translational gap" between basic science and clinical practice[25, 26]. Addressing this gap may require more rigorous evaluation of experimental models besides the refinement of research questions in order to successfully develop novel therapies.

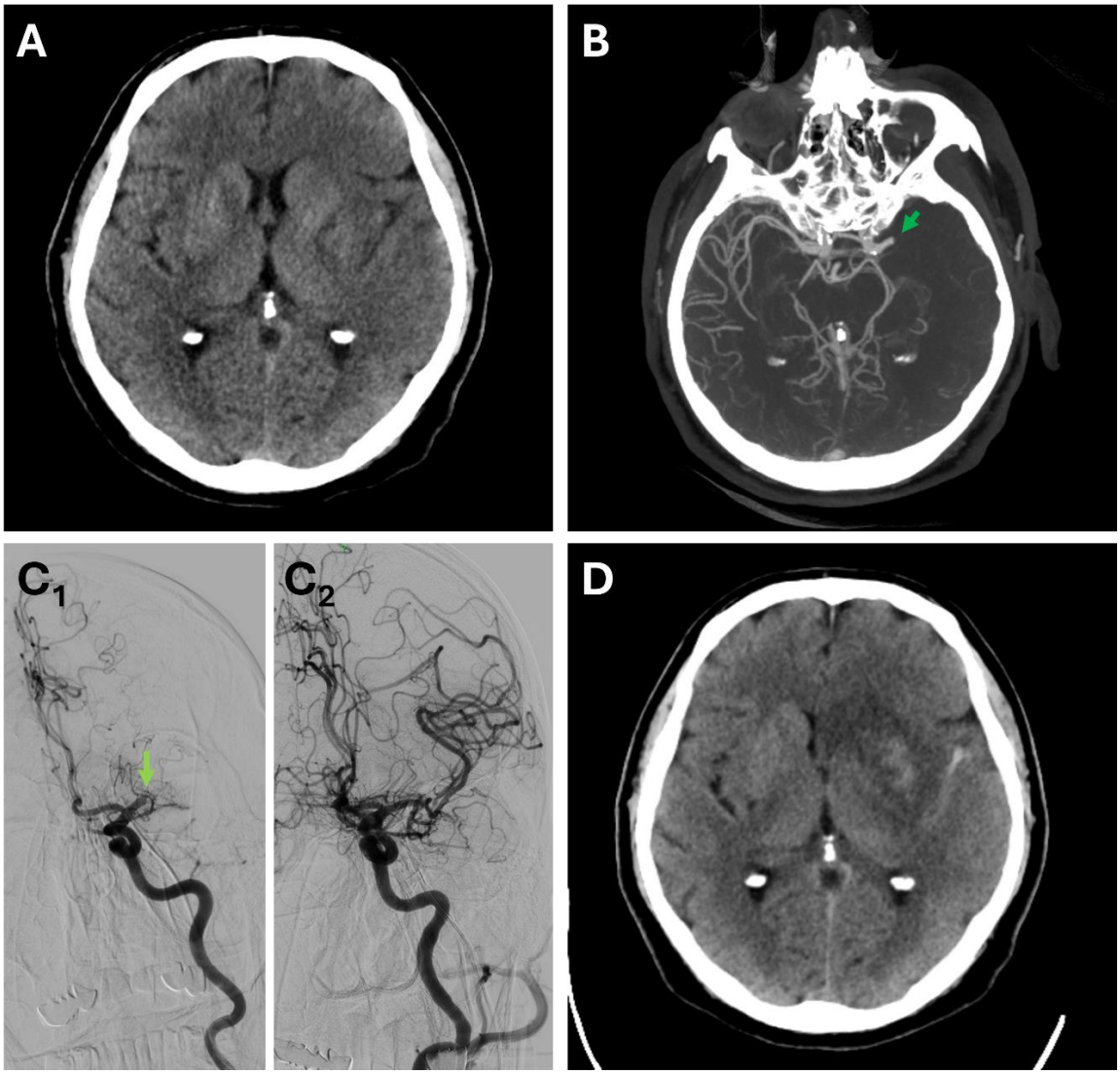

Figure 3. Infarct evolution and concomitant cerebral edema progresses despite successful endovascular recanalization. **A,** In the native CT scan, early signs of ischemia are visible in the left insular and cortical regions, supplied by the middle cerebral artery (MCA). **B,** In the angiographic scan, occlusion in the proximal segment of the left MCA appears as a filling defect of the vessel (green arrow). **C_1,** Left MCA occlusion is verified by Digital Subtraction Angiography (green arrow). **C_2,** Following successful thrombectomy, the perfusion in the MCA and its branches is restored. **D,** Despite complete and timely recanalization, the 24-hour control CT shows progression of the infarct in the cortical and subcortical areas of the MCA territory. Subtle midline shift, compression of the

left lateral ventricle and narrowing of surface liquor spaces are consequences of cerebral edema concomitant to ischemic injury. Representative images are courtesy of the Department of Radiology, Albert Szent-Györgyi Healthcare Centre, Szeged, Hungary.

Secondary pathophysiological mechanisms – spreading depolarization

While primary infarct size is essentially determined by the duration of ischemia and the collateralization of the affected brain territory[27, 28], secondary pathological mechanisms occur shortly after this initial ischemic insult and promote lesion progression by transforming the penumbra region into unsalvageable core[29, 30].

Spreading depolarizations (SD) of the cerebral cortex are waves of near-complete depolarization of neurons and glial cells that arise spontaneously and propagate at a speed of 2–6 mm/min through the grey matter. Passage of SDs is followed by transient silencing of neuronal activity. SDs impose a heavy metabolic load on neural tissue during their transit, as they are the most energy-intensive neurophysiological phenomenon that can occur in the cortex[31]. During an SD, the neurons lose their resting membrane potential as the transmembrane ion gradient nearly equilibrates due to a large amount of K^+ escaping into the extracellular space, while Na^+ and Ca^{2+} enter the cells driven by their concentration gradient[32]. The restoration of membrane potential exhausts the tissue's energy reserves and deepens the metabolic crisis, reducing the nervous tissue's chances of survival with each passing SD. Furthermore, the reorganization of ions results in a concomitant vascular response to the depolarization wave and causes cellular swelling at the same time.

In 1944, Aristides A.P. Leão discovered a transient decrease in cortical activity spreading in a wave-like manner in the rabbit cerebral cortex. He observed a transient, marked reduction in the amplitude of spontaneous oscillations in the electrocorticogram and named the phenomenon 'spreading depression'[33]. Despite the similarities, transient periinfarct depolarizations occurring after ischemic brain injury, as well as terminal depolarization of neurons following severe oxygen depletion, were thought to be completely different entities. However, numerous studies to date have demonstrated that artificially induced spreading depolarization waves in physiological tissue and peri-infarction depolarization are essentially different forms of the same phenomenon[31, 34]. According to the current view, the term SD thus refers to a continuum ranging from transient SD in metabolically intact nervous tissue to terminal SD in severely ischemic cortex (Fig. 4). Consistent with this concept, SDs appear in migraine auras as well as in serious diseases leading to neurological deficits, such as subarachnoid hemorrhage, traumatic brain injury, circulatory arrest, and the aforementioned ischemic stroke[35-37]. Just like in animal

models, SDs can be detected and used as biomarkers of injury progression in critical care patients following central nervous system (CNS) injury[38].

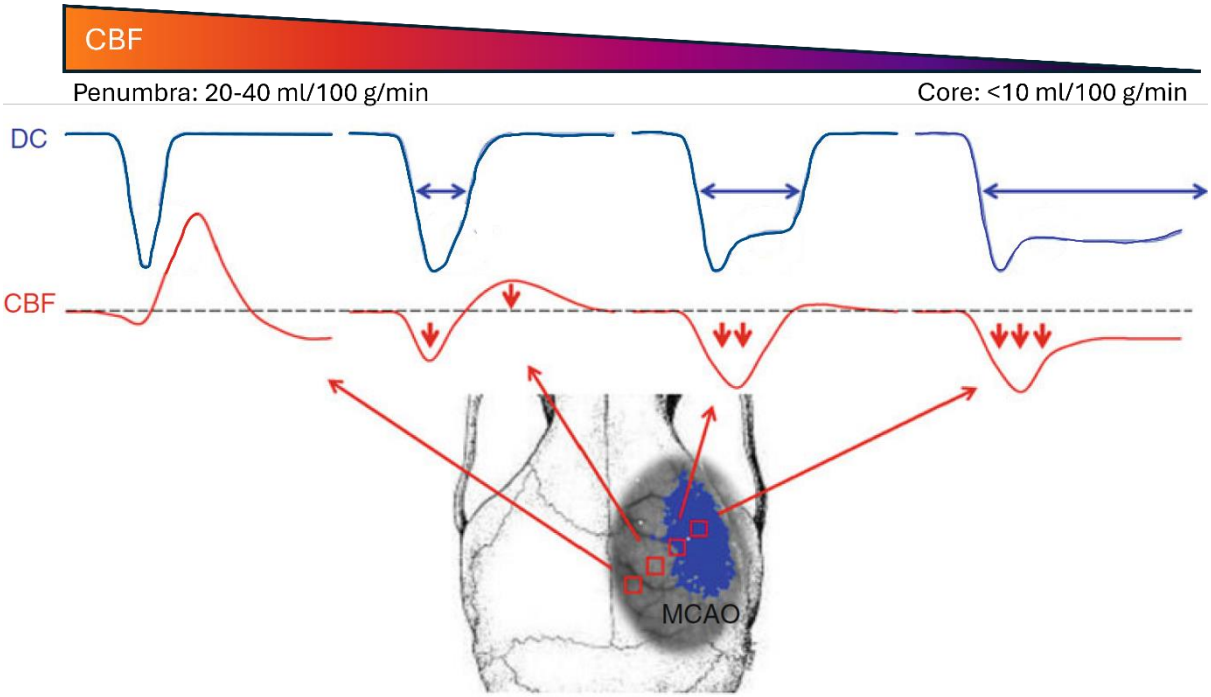

Figure 4. Nature of the cerebral blood flow (CBF) response to spreading depolarizations (SD) depends on the metabolic state of the ischemic cerebral tissue. Representative traces of direct current (DC) potential characteristic to SD (blue traces) and accompanying CBF changes (red) display different morphology as a function of tissue perfusion. Traces correspond to squares over the schematic drawing of ischemic rodent brain from left to right, from penumbra towards core, respectively. Figure was adapted and modified from Hoffmann and Ayata, 2013.

In the case of ischemic stroke, SDs originate from the margin of the core and spread through the penumbra, causing deleterious effects that endanger the survival of the tissue that is still salvageable. The blood flow response associated with SD consists of different phases, which may occur to varying degrees depending on the metabolic state of the nervous tissue[39, 40]. The typical CBF response is characterized primarily by hyperemia, which is preceded by transient hypoperfusion and followed by a prolonged period of oligemia. The excess nutrients arriving with the increased blood flow promote the restoration of cell homeostasis and thus benefit the tissue. However, the altered metabolic state of ischemic tissue promotes the deepening and prolongation of initial hypoperfusion at the expense of hyperemia. In highly metabolically challenged tissue, CBF response may consist only of vasoconstriction, termed spreading ischemia[32] (Fig. 4). Consequently, in the ischemic cerebral cortex with a lower baseline flow, further reduction in CBF jeopardizes the survival of cells already in a critical state due to ischemia and may contribute to the transformation of the penumbra region into the core region[41]. In case of a prolonged depolarization, harmful high intracellular Ca^{2+} and Na^{+} concentrations and cytotoxic edema also persist for a longer period[42].

As cells of the cerebral cortex depolarize, positive cations enter the intracellular space, pulling water into the cell and creating cellular swelling called cytotoxic edema[43]. SDs are known to cause cytotoxic edema and in turn, cytotoxic edema is proven to promote SD evolution[29]. This reciprocal interaction creates a self-amplifying vicious cycle that triggers the cascade of edema formation following ischemic stroke[44, 45].

Secondary pathophysiological mechanisms – edema formation

Cerebral edema and consequent brain swelling are complications arising from ischemic stroke, which promote further tissue injury[44] (Fig. 3&5). Malignant cerebral edema (CE), describing the detrimental swelling of brain tissue in the MCA territory with midline shift and possible brain herniation, is a such consequence, evolving in 7-18% of the patients over two-three days. Mortality of CE lies at 80-85% and is a prognostic factor of unfavorable outcome due to its negative correlation with the probability of recovery[46, 47]. The conventional interventions are typically reactive rather than preventive and only fight against the late- and lethal complications of CE[48]. Yet, no treatment focuses on the CE prevention in acute stroke. Since current clinical guidelines lack routine anti-edema therapy[14, 49, 50], there is a pressing need for proper medication against CE in the acute phase of stroke. Therefore, detailed investigation of the exact mechanism of edema formation is essential.

The evolution of cerebral edema can be divided into distinct phases based on the pathomechanism. These phases appear in a specific order and then continue to occur in parallel with each other[44, 51].

The first phase, cytotoxic edema occurs within minutes of an ischemic insult (Fig. 5) and is triggered by an acute tissue deprivation of glucose and oxygen, as well as the appearance of spreading depolarizations[43, 52]. Due to ATP depletion, the energy intensive transmembrane pumps are not able to maintain transmembrane ion gradients. Therefore, osmolytes start to move according to their electrochemical gradient, which is the driving force for large amounts of extracellular Na^+ and Cl^- followed by water to enter the intracellular space. Although depolarizations affect both cell types, neurons are devoid of water channels, hence cytotoxic swelling affects mostly astrocytes that have four times higher water permeability due to water channels[53]. Since water and solute translocation occurs solely between the intracellular space and the extracellular interstitial fluid, there is no net growth in tissue volume.

The massive influx of Na^+ ions into the cells depletes the interstitial fluid of its ion stock, consequently the change in ion concentration creates a newly established driving force for Na^+

from the intravascular space into the brain parenchyma. Cl^- and water follow as secondary participants in order to maintain electrical and osmotic neutrality[44, 51]. Since the driving force in the phase is the movement of ions, it was termed ionic edema. Since in this phase, the blood-brain barrier (BBB) is still intact, entry of water can only happen transcellularly through the vascular endothelium, either by diffusion through the plasma membrane or through water permeable channels, similar to the swelling of astrocytes. This phase of edema already results in net volume growth, since excess water enters the brain parenchyma, but for that active blood flow is required[52]. In the acute setting of stroke, blood flow in the core region is, by definition, severely reduced to levels approaching zero. Consequently, water entry occurs primarily in the penumbral zone, where circulation is relatively preserved, and subsequently moves into the core region by bulk flow.[44]. Another possibility is that the previously ischemic area becomes reperfused, leading to water entry directly at the site of the ischemic core.

For many years it was believed that the exclusive source of water entering the brain interstitium was the intravascular space. In the early 2010s a new paravascular way of effective solute transportation in the cerebrospinal fluid (CSF) was described and named the glymphatic system[54, 55]. Studies following the discovery proved that fluid from the Virchow-Robin space enters the brain parenchyma earlier, than intravascular water does, emphasizing the role of CSF flux in ionic edema formation[45]. Convective flux of CSF along the vasculature is physiologically maintained by breathing, arterial pulsatility and the constant water-buffering of astrocytes[55]. In the setting of ischemic stroke, the spontaneously appearing SDs cause dynamic alterations in vascular diameter and consequently hydrostatic pressure in the paravascular space. This pressure change pulls in more CSF from the intact regions into the injured brain areas, presenting an additional mechanism of how SDs contribute to secondary lesion progression and poor outcome following stroke[45].

Brain swelling peaks 2-3 days following an ischemic insult (Fig. 5), which coincides with the break-down of the BBB following the progressive alteration of the barrier's permeability due to edema and occasional reperfusion[45, 51]. Vasogenic edema formation is characterized by the opening of paravascular pathways due to the failure of intercellular anchors and the degradation of the basement membranes by enzymes activated in inflammatory cascades, like matrix metalloproteases. An ultrafiltrate of blood containing macromolecules can enter the brain, pulling in vast amounts of water dictated by pressure differences, creating space-occupying edema. The final stage of endothelial dysfunction is a catastrophic breakdown of capillary integrity, during which all components of the blood, including erythrocytes, leak into the brain

parenchyma, causing hemorrhagic transformation[44]. This devastating complication occurs in up to 30-40% of ischemic strokes.

Conventional, reactive anti-edema interventions mainly target vasogenic edema rather than cytotoxic edema, despite evidence that cytotoxic edema is an early event following brain injury, precedes vasogenic edema, and promotes its subsequent formation[53, 56]. To conquer this obstacle, alternative, more targeted anti-edema therapies should be developed, which focus on preventing edema formation in the early, namely cytotoxic phase.

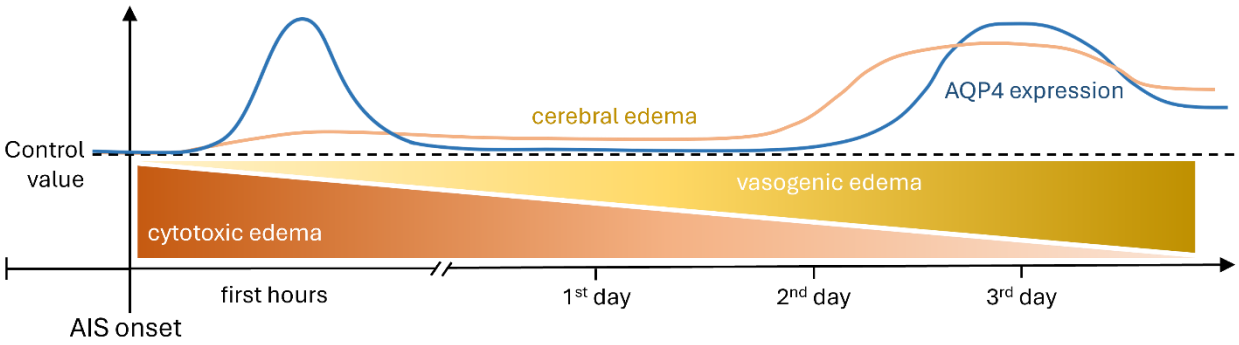

Figure 5. Cerebral edema formations occurs seconds after the onset of ischemia and progresses into vasogenic edema over time, peaking 2-3 days following injury. At the same time, ischemia drives bi-phasic upregulation of the water channel aquaporin-4 (AQP4) with an early peak that contributes to cytotoxic swelling, followed by a later, sustained increase at 24–48 hours coinciding with vasogenic edema and edema resolution [57, 58].

AQP4 - a target for edema regulation?

Astrocytes are one of the main cell types of the CNS, serving several functions in order to maintain the well-regulated homeostasis for the ideal functioning of neurons. On the one hand, they cover almost the entire cerebral vascular system with their endplates[51], thereby not only participating in the creation of the blood-brain barrier, but also creating the perivascular space around the blood vessels[59], which is essential for the glymphatic system[55] and is the location for neurovascular coupling. Although astrocytes are single cells, they are coupled to each other by gap junctions (GJ) to create a functional syncytium. GJs enable astrocytes to allow free ion flow in accordance with the concentration gradient between cells, allowing effective uptake, distribution and buffering of K^{+}[60], neurotransmitters, several other solutes and importantly, water.

Movement of water into astrocytes is facilitated through three different routes under physiological conditions following transmembrane ionic gradient[51]. First is simple diffusion through the lipid bilayer. Second are water permeable transporters that are constitutively expressed on astrocytes, like NKCC1 and glutamate transporters EAAT1 and EAAT2. The most important pathway is through dedicated water channels, namely aquaporin-4 (AQP4). Out of

the three isotypes of the aquaporin family expressed in the central nervous system, AQP4 is specific for astrocytes[51]. AQP4 expression is especially prominent at astrocytic perivascular end-feet (Fig. 6), where they are assembled into large multimeric complexes called orthogonal arrays of intramembranous particles (OAPs)[51], which cover almost 40% of glial end-feet[55]. The channels mediate osmotically driven, bidirectional water movement between the bloodstream or cerebrospinal fluid in perivascular spaces and the brain parenchyma[61], and build the anatomical basis for continuous flow in the glymphatic system[55]. Furthermore, they are coupled with potassium channels and therefore are key to K^+ spatial buffering[62].

AQP4 plays a central role in the development of cytotoxic edema, as demonstrated by studies in AQP4 knockout mice, in which ischemia-induced brain swelling was reduced by approximately 35% compared with wild-type controls[63]. In the setting of stroke, AQP4 expression is upregulated in a biphasic manner, as the first phase develops one hour after the onset of ischemia, followed by a second peak 48–72 hours later[64, 65] (Fig. 6). Besides the enlarged pool of water channels, the sulfonylurea receptor 1 (SUR1)-transient receptor potential melastatin 4 (TRPM4)-AQP4 complex, which assembles only under pathological conditions, has been identified as a major route of bulk water influx driving astrocyte swelling[66, 67].

For these reasons, pharmacological modulation of AQP4 has emerged as a promising strategy to limit brain edema formation by restricting pathological water influx. Direct pharmacological blockade of AQP4, however, may be counterproductive due to the dual role the channels[68]. AQP4 contributes not only to cytotoxic edema formation but also to edema resolution, therefore the water flux through the channels can be deleterious during edema formation, but beneficial during the resolution phase[58]. Since permanently suspended AQP4 function delays water resorption to cerebral vessel and exaggerates vasogenic edema[69, 70], as an alternative approach, reversible modulation of AQP4 subcellular localization focused on the hyperacute phase of injury, rather than pore blockade, has been proposed. This concept is supported by observations showing that both AQP4 expression and its membrane distribution are altered in astrocytes exposed to hypotonic stress and in the mouse cortex following acute brain injury[71, 72]. In primary cortical astrocyte cultures, exposure to hypotonic conditions or mechanical impact increased the relocation of AQP4 from intracellular vesicles to the plasma membrane[71, 72]. Furthermore, in the setting of AIS, AQP4 distribution becomes dysregulated, polarization to the end-feet is lost and the channels are become distributed evenly around the plasmalemma[73] (Fig. 6) - the proteins of the dystrophin-associated protein complex (DAPC) anchoring AQP4 OAPs to the astrocyte end feet are sensitive to ischemia and disassemble upon injury[74]. AQP4

mislocalization can persist for almost a month after injury[55]. Therefore, inhibiting AQP4 translocation during the hyperacute phase of AIS may prove beneficial.

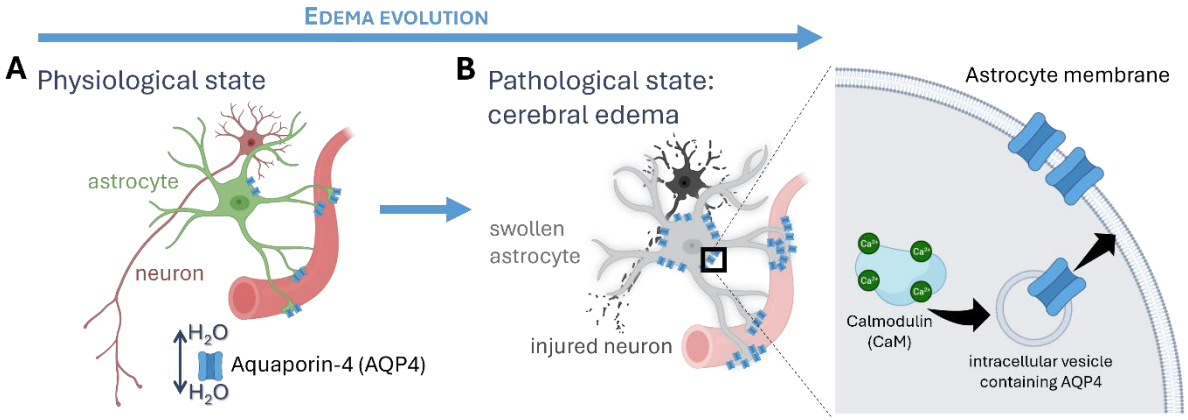

Figure 6. Edema evolution is linked to astrocyte swelling, AQP4 upregulation and dysregulated translocation to the membrane. **A,** Under physiological conditions, AQP4 is polarized to the astrocyte end-feet. **B,** Following ischemia, polarization of AQP4 is lost and a pool of over-expressed, mislocalized channels contribute to cytotoxic swelling. The trafficking of AQP4 is dependent on calmodulin (CaM) function. Figure was adapted and modified from Kitchen et al, 2020.

The translocation of AQP4 from intracellular vesicles to the plasma membrane has been linked to increases in intracellular Ca^{2+} concentration and the activation of Ca^{2+}-dependent calmodulin (CaM)[58, 71] (Fig. 6). CaM drives AQP4 translocation in both direct and indirect manners[75], therefore plays a central role in the process. Besides compounds traditionally used for the purpose of kinase inhibition[76], a new candidate drug was recently introduced[75]. Trifluoperazine (TFP) is a patented, FDA-approved antipsychotic and anxiolytic agent used in clinical practice for the treatment of schizophrenia. The beneficial properties of the drug in psychiatry are attributable to its antagonistic effect on D2 dopamine and α1-adrenergic receptors, but it also has a known CaM inhibitory effect. Notably, AQP4 translocation to the astrocytic membrane was inhibited by TFP[75]. Furthermore, TFP administration reduced edema formation and improved functional outcomes in a rodent model of spinal cord injury[75] and in the photothrombotic mouse model of stroke[77]. Collectively, these findings suggest that pharmacological inhibition of AQP4 translocation to the astrocyte surface may represent a novel therapeutic approach for mitigating cerebral edema[67].

Secondary pathologies form a mutually reinforcing cascade in ischemic stroke. SDs drive cytotoxic edema by triggering massive ionic influx and water entry into astrocytes - processes facilitated by AQP4 water channels at their end-feet. The resulting swelling further promotes SD generation, tightly coupling these secondary injury pathways and accelerating metabolic failure in the penumbra. Through this SD-AQP4-edema feedback loop, SDs effectively act as the central mechanism linking early cytotoxic edema to later stages of edema progression.

HYPOTHESIS AND AIMS

Our group has shown that spreading depolarizations (SDs) cause cytotoxic astrocytic swelling, which increases tissue susceptibility to subsequent SDs and contributes to astrocyte dysfunction and injury progression[29]. Because aquaporin-4 (AQP4) channels mediate the main route of water entry during early ischemic injury, we aimed to influence AQP4 trafficking by targeting its Ca^{2+}-dependent regulatory pathway through calmodulin (CaM) inhibition. To achieve this, the work was structured around the following objectives:

1. Characterization of astrocytic Ca^{2+} dynamics during spreading depolarizations (SDs). Given that intracellular Ca^{2+} elevation is a key trigger for AQP4 trafficking, this objective focused on defining the spatiotemporal profile of astrocytic Ca^{2+} signals during SDs using multiphoton microscopy.

2. Pharmacological suppression of Ca^{2+}-dependent signaling and evaluation of its functional consequences. This objective used trifluoperazine (TFP) to inhibit calmodulin (CaM) and evaluate how suppressing Ca^{2+}-dependent signaling affects SD susceptibility and associated CBF responses. We then assessed TFP's effects in a filament MCAO mouse model on neurological outcomes, neurovascular coupling, and infarct features— including infarct volume, edema, and blood–brain barrier integrity—using MRI and SPECT.

Finally, our pharmacological analyses revealed a paradoxical, non-linear relationship between infarct volume and neurological deficit. This unexpected finding prompted the development of a separate project, which became a third, supplementary aim of the thesis.

3. Characterization of the relationship between infarct volume and the corresponding neurological deficit following MCAO in mice. Based on MRI-measured infarct volumes and the evaluation of neurological deficits in mice, we analyzed the correlation between these two parameters and confirmed their relationship.

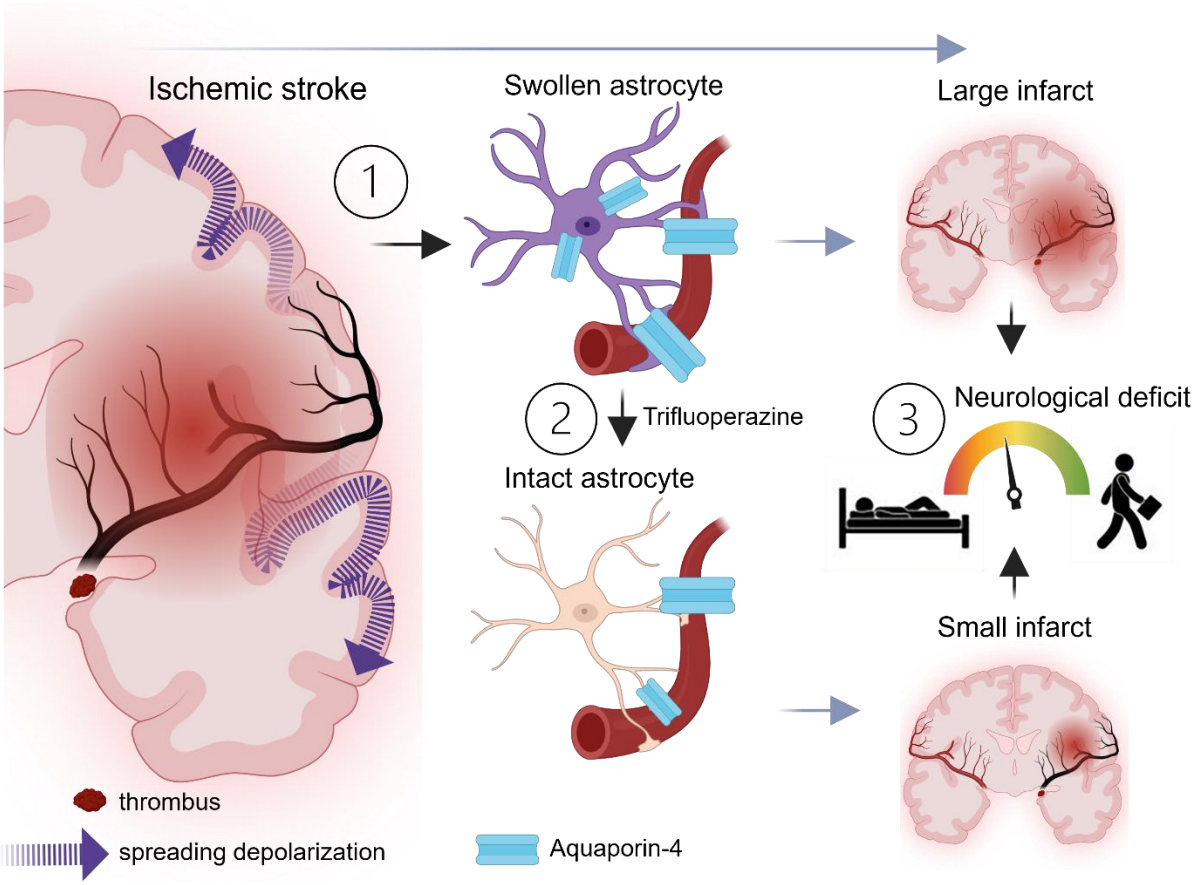

Figure 7. Graphical representation of the study aims. The numbers indicated in the figure correspond to the list of aims outlined in the text.

MATERIALS AND METHODS

Animals

Adult male C57BL/6 mice (Charles River Laboratories; 2–4.5 months old; weighing 26.83 ± 3.91 g) from the husbandry facility of the Biological Research Centre, Szeged, Hungary, were used in this study. All experimental procedures were conducted in strict accordance with the guidelines of the National Food Chain Safety and Animal Health Directorate of Csongrád County, Hungary (Ref. no. II./1234/2025, XXXII/4050/2020 and I-74-23/2022), and the Scientific Committee of Animal Experimentation of the Hungarian Academy of Sciences (updated Law and Regulations on Animal Protection: 40/2013. (II. 14.) Gov. of Hungary), following EU Directive 2010/63/EU on the protection of experimental animals. The study adhered to established ethical guidelines, and the experiments are reported in compliance with the ARRIVE guidelines[78]. The animals were housed under controlled environmental conditions (temperature: 23 °C; humidity: constant; light/dark cycle: 12 h/12 h, lights on at 7 a.m.). Standard rodent chow and tap water were provided *ad libitum*.

Anesthesia during surgical procedures and data acquisition

Mice were anesthetized with isoflurane vaporized in a humidified gas mixture of O_2:N_2O (1:2), with 4% isoflurane for induction and 0.5-1.5% for maintenance and allowed to breathe spontaneously through a nose cone. The depth of anesthesia was assessed repeatedly by leg pinching and the amount of anesthetic was adjusted accordingly. Body temperature was maintained at 37°C by continuous monitoring using a rectal probe connected to a feedback-controlled heating pad (CODA® Monitor, Kent Scientific Corporation, 1116 Litchfield Street, Torrington, CT 06790, USA). The protocol was applied during all surgical procedures, unless stated otherwise.

Surgical preparation for astrocyte Ca^{2+} imaging

Mice (n=6) were anesthetized with 1% Avertin (20 L/g, i.p.) and mounted on a stereotactic frame incorporating a heating pad. A cranial window (d=3 mm) was prepared on the right parietal bone, and the dura was retracted. For astrocyte intracellular calcium imaging, the exposed brain surface was first loaded topically with a green, fluorescent calcium indicator Fluo 4-AM (45 M in aCSF, Thermo Fisher, Waltham, MA, USA) and incubated for 15 min. Subsequently, to label astrocytes, the red fluorescent dye sulforhodamine 101 (SR101, 80 M in artificial cerebrospinal fluid (aCSF), Thermo Fisher, Waltham, MA, USA), was applied topically, and left on the brain surface for a further 15 min. A perceived limitation of our SR101

labeling protocol may be the potential non-specific cellular uptake of the dye[79]. We identified cells selected for the analysis as astrocytes on the basis of their morphology (e.g., ramified structure, endfoot processes embracing vessels) in the superficial layers of the cortex, which is particularly rich in astrocytes due to the formation of the superficial glial limiting membrane. Although the labeling of oligodendorcytes cannot be excluded, oligodendrocytes display round somata, and the superficial layer of the cortex examined here has been known to be largely devoid of oligodendrocytes[80]. The predominant uptake of the dye by astrocytes, in contrast with neurons, was also substantiated by the obvious, dark shadow of neuronal cell bodies in the neuropil in the preparations. The craniotomy was then closed with a microscopic cover glass. A second, smaller trepanation was drilled rostral to the first craniotomy, to be used for SD elicitation. A glass capillary connected to a syringe pump (CMA/100, CMA/Microdialysis, Solna, Sweden) was filled with 1 M KCl, and was fastened to the skull with acrylic dental cement, with its tip positioned at the cortical surface within the rostral trepanation.

Multiphoton microscopy

Multiphoton excitation was performed at the 810 nm wavelength according to protocols described previously[81]. In vivo intracranial microscopy was performed with a FEMTO 3D Dual microscope (Femtonics Ltd., Budapest, Hungary) using a 20× large working distance water objective (XLUMPLFLN-20XW, Olympus, Tokyo, Japan) and MES software (v4.6.2336, Femtonics, Budapest, Hungary). Two-photon excitation was performed with a Mai Tai HP Ti-sapphire laser (RK TECH Ltd., Budapest, Hungary) at 810 nm, which was found optimal for Fluo-4 AM excitation, and adequate for SR101. Emission was detected with gallium arsenide phosphide photomultipliers, equipped with the appropriate color filters. Laser power was set to 10–40%, depending on the depth of imaging (0–300 μm from the brain surface), photomultiplier voltages were set to 70%. Final imaging depth in the somatosensory cortex was 55–85 μm, where a z-stack with 5 μm vertical steps was recorded at the area of interest for the identification of astrocytes. Image sequences were taken of the desired cells at approximately 1 μm/pixel spatial and 0.8–2.5 Hz temporal resolution. After acquiring baseline images, SD was triggered repeatedly at intervals of 15–20 min in the rostral cranial window by the ejection of 1–3 μL 1 M KCl to the brain surface through the glass capillary. SD evolution was confirmed by the occurrence of synchronous, propagating astrocytic calcium waves (Fluo 4-AM intensity increase, green channel) and the associated changes in arteriole diameter.

SD susceptibility testing

Mice (n=18) were anaesthetized according to the protocol detailed above. After topical application of lidocaine (1%) to the ear canals, the animals' heads were mounted in a stereotactic frame. Under local anesthesia (lidocaine 1%), an incision was made in the midline of the scalp, and the skin was retracted laterally. Two open craniotomies were made over the parietal cortex: a larger window was placed rostrally for recording, while a smaller one was drilled for SD elicitation. The windows were continuously flushed with artificial cerebrospinal fluid (aCSF) (composition of aCSF in mM concentrations: 126.6 NaCl, 3 KCl, 1.5 $CaCl_2$, 1.2 $MgCl_2$, 24.5 $NaHCO_3$, 6.7 urea, 3.7 glucose bubbled with 95% O_2 and 5% CO_2 to maintain a constant pH of 7.4). A laser Doppler flow probe was positioned in the cranial window to measure local cerebral blood flow. Two microcapillaries with Ag/AgCl electrodes were also placed in the cranial window for local field potential (LFP) acquisition, filtered in direct current (DC) mode (<1 Hz), with the reference electrode implanted under the skin of the animals' neck.

After recording a 10-min baseline, 20 µM TFP solution in aCSF was applied topically in both the acquisition and elicitation windows in treated animals (n=8), while only the solvent was applied in the control group (n=10). During the 20-minute incubation period and throughout the elicitation of SDs, the solutions were renewed every 10 minutes.

SDs were elicited by topical application of 1M KCl in the caudal window, renewed every 15 minutes for the 120 minutes of data acquisition.

Modified filament middle cerebral artery occlusion (MCAO)

Mice (n=69) were anesthetized according to the protocol detailed above. To verify sufficient reduction of cerebral blood flow (CBF) during MCAO, after a midline scalp incision and lateral skin retraction on the left side, a laser Doppler probe was fixed to the parietal bone of the skull over the cortical area supplied by the MCA.

To model ischemic stroke, transient intraluminal filament occlusion of the left middle cerebral artery (MCAO) was performed according to a modified version of the Koizumi method[82]. Modifications were made to allow complete reperfusion of all branches of the internal and external carotid arteries. Following disinfection with pure ethanol and local anesthesia with 1% lidocaine, a midline incision was made from the chin to the jugulum. Blunt dissection was used to free the left common carotid artery, the carotid fork and the proximal segments of the internal and external carotid arteries from the surrounding tissues, and the vagal nerve was gently isolated. A fine silk thread (Fine Science Tools, USA) was looped around the external carotid

artery, the thread was secured with arterial forceps and the vessel was pulled aside to transiently stop blood flow. A microclip (Fine Science Tools, Inc. 4000 East 3rd Avenue, Suite 100 Foster City, CA 94404-4824, USA) was placed on the common carotid artery. A small hole was punctured in the common carotid artery distal to the microclip using a 30G curved-tip needle. A silicone-coated 230 µm microfilament (Doccol Corporation, 30 Eisenhower Drive, Sharon, MA 02067-2427, USA) was then advanced through the incision and up the internal carotid artery until it reached the origin of the middle cerebral artery, indicated by a sudden resistance. Occlusion of the MCA was also confirmed by a drop in CBF to less than 20% of baseline, as measured by the Doppler probe.

Ischemia was maintained for 60 minutes. Reperfusion was induced by retracting the filament, then a small piece of gelatin sponge (Gelita Tampon, B. Braun Surgical, S.A., Carretera de Terrassa, 121, 08191 Rubí, Spain) was placed over the wound on the common carotid artery and the vessel was also compressed until bleeding ceased completely. The microclip was removed 10 minutes after reperfusion and the external carotid artery was also recanalized. The neck and scalp wounds were surgically sutured and disinfected with Betadine solution. The mice were transferred to an incubator cage (30°C) until they regained full consciousness and were then reunited with their original cage mates.

Post-operative care and management

During the 72-hour post-MCAO survival period, comprehensive postoperative care included the provision of food, water, and nutritional supplements as recommended by Lourbopoulos et al.[83] and Pinto et al.[84], as well as analgesia. Immediately after surgery, the non-steroidal anti-inflammatory drug carprofen was administered subcutaneously (5 mg/kg) (Rycarfa, Tolnagro, 7100 Szekszárd, Hungary) and repeated every 12 hours. For fluid and electrolyte supplementation, 0.3 ml of 5% glucose solution (in 0.9% NaCl solution) and 0.3 ml of a 50-50% mixture of Duphalyte (Zoetis Hungary Kft., Budapest) and physiological saline were given subcutaneously twice daily. *Ad libitum* access to dry and soaked pellet food and DietGel® Recovery (ClearH2O, 85 Bradley Drive, Westbrook, ME 04092, USA) was provided, complemented by *per os* siringe feeding of gelatinised pellet food.

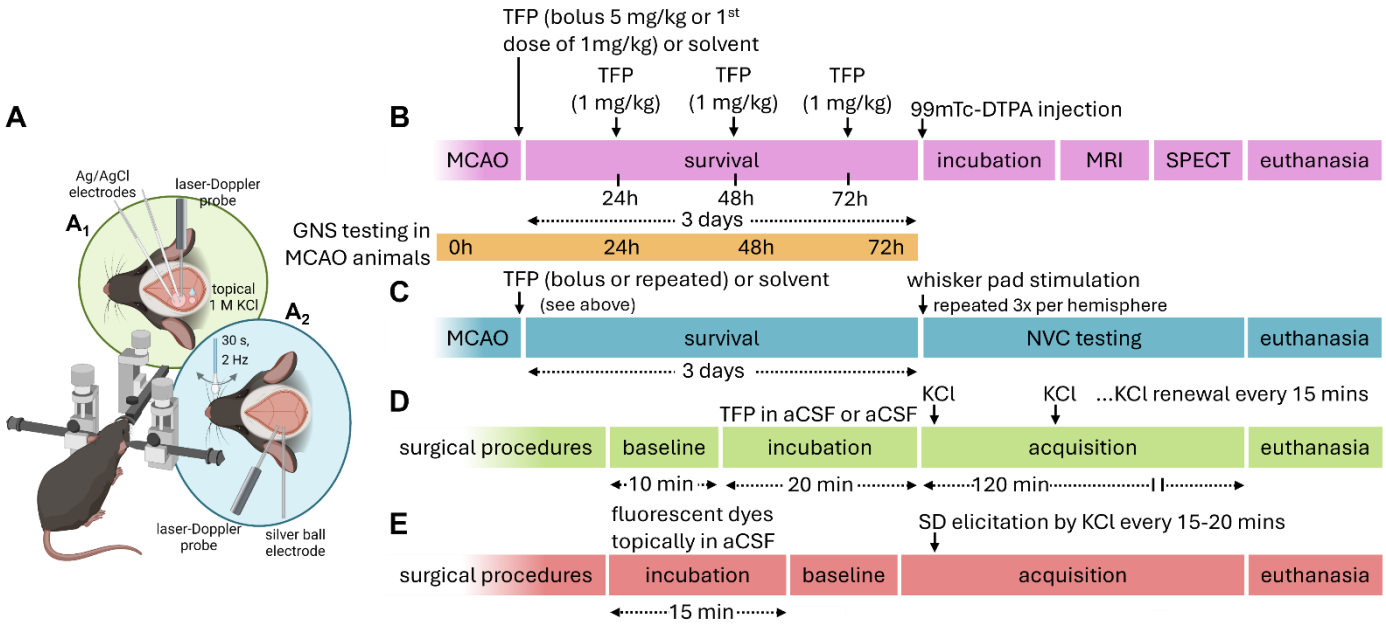

Figure 8. Experimental protocols for experiments including multimodal imaging (**B**) and whisker-pad stimulation (**A$_2$** and **C**) following MCAO, SD susceptibility testing (**A$_1$** and **D**) and astrocyte imaging with multiphoton microscopy (**E**) in the non-ischemic mouse cortex.

Pharmacological treatment

Trifluoperazine (TFP) is an antipsychotic drug used primarily in the treatment of schizophrenia. As a repurposed compound, TFP is being used experimentally across a wide range of indications due to its inhibition of the calcium-binding protein, calmodulin (CaM). CaM is proposed to play a regulatory role in AQP4 trafficking between intracellularly stored and cell membrane-expressed channels; hence, TFP was used to modulate cell surface AQP4 expression.

Experimental animals were divided into two separate experimental groups to test two different dosing protocols. The first group (n=14) was treated with 1 mg/kg TFP subcutaneously after complete recanalization of the MCA. Treatment was repeated every 24 hours, with animals receiving the final, 4th dose at 72 hours of survival. The second group (n=13) was treated with a single dose of 5 mg/kg TFP immediately after recanalization. Animals of the control group received the solvent 0.9% NaCl subcutaneously (n=14).

Neurological testing

Animals underwent neurological testing 24 hours prior to surgery, and daily from 24 to 72 hours after MCAO. The Garcia Neuroscore Scale (GNS), a scoring system specifically designed to evaluate sensorimotor deficits following ischemic brain injury in rodents was utilized[85]. The GNS score ranges from 0 (severe deficit) to 21 (no deficit). All test domains were performed in the same order for each animal with three investigators present at a time to ensure unbiased scoring.

Neurovascular coupling testing by whisker stimulation

To assess the status of the neurovascular unit (NVU), neurovascular coupling (NVC) was tested by mechanical whisker stimulation. Mechanical stimulation of the whiskers induces an increase in cortical perfusion - called functional hyperemia - in the contralateral somatosensory barrel cortex, that maps the whiskers. The characteristics of functional hyperemia are descriptive of the efficacy on NVC and the condition of the nervous tissue.

After 72 hours of survival, neurovascular coupling was tested in the animals (n=19). Anesthesia was induced according to the protocol detailed above. The animal's head was fixed in a stereotactic frame, the scalp was incised and the skull exposed. First, a laser Doppler probe was placed over the barrel cortex on the parietal bone with a silver ball electrode in close proximity.

Isoflurane is known to have pronounced vasodilatory effect. Therefore, to record the functional hyperemia that develops on basal vascular tone, the anesthetic had to be changed to a drug without vascular effects. Before the start of the NVC test, anesthesia was switched from isoflurane alone to medethomidine (0.1 mg/kg i.p.), supplemented by a reduced amount of isoflurane (0.1%) to maintain proper baseline vascular tone but maintain analgesic effects.

After reaching a stable baseline, mechanical whisker stimulation was performed at a frequency of 2-5 Hz for 30 seconds, repeated at least 3 times with 2-minute intervals to allow CBF to fully recover in between. The test was repeated in the same way in the other hemisphere spared from ischemia to serve as control.

MRI and SPECT imaging

MRI and SPECT imaging were performed in 21 animals at 72 hours survival. [^{99m}Tc]DTPA (Medi-Radiopharma Co Ltd., Hungary) was administered intravenously (76.03 MBq ± 34.23 MBq activity in 30-100 µl solution) 2 hours prior to the start of the SPECT imaging via tail vein injection. Animals were kept awake for an hour and then anaesthetized by isoflurane for the imaging studies. The animals were placed on a heated pallet during scanning, and 1,5-2% isoflurane was used for the maintenance of anesthesia. Respiration rate and the temperature were continuously monitored, and isoflurane concentration was adjusted accordingly.

First MRI scans were acquired using a Mediso NanoScan PET/MRI 3T system (Mediso Ltd., Budapest, Hungary) equipped with a maximum of 450 mT/m gradients. A dedicated mouse head volume coil (inner diameter 30 mm) was used for both transmission and reception. The T2-weighted fast spin echo scan was acquired with a three-dimensional acquisition scheme and the following parameters: 35 × 35 mm field of view, 220 × 220 acquisition matrix size, and 96

adjacent slices of 0.2-mm slice thickness. The echo-train length was set to 96, the echo time was 69 ms and the repetition time was 2 s with one average to deliver a total acquisition time of ~6.5 min. The diffusion-weighted scan consisted of two b-values (b = 0 and 800 s/mm2, δ = 2.4 ms, Δ = 12 ms) along three perpendicular directions, each repeated fourteen times. The study utilized the spin-echo echo-planar imaging pulse sequence to produce high-quality images of 22 adjacent slices (0.7 mm thickness) within a total acquisition time of 10 minutes. The field of view was set at 25 × 25 mm, and the acquisition matrix was optimized at 80 × 80. The echo time was set at 59.1 ms using 300-kHz bandwidth and repetition time 5 s. To ensure accuracy, susceptibility and eddy current distortion corrections were applied during the reconstruction based on reference echo scans. ADC values were calculated for the lesion, the whole ipsilateral hemisphere to stroke, and the whole contralateral intact hemisphere using InterView Fusion software (Mediso, Hungary). Hemispheric volumes (HV) and lesion volumes (LV) were calculated from the T2FSE sequences and ADC maps.

MRI scans were immediately followed by the SPECT/CT measurements, performed on a nanoSPECT/CT (Mediso Ltd., Hungary) equipped with multi-pinhole collimators. Head SPECT scanning was performed with 30 frames per cycle and termination condition of 120 s per frame in a scan range of 26.8 mm. The SPECT reconstruction was set to have 0.2 mm isovoxels while the field of view was centered to the head. The results of SPECT measurements were quantified in units of radioactivity measured per unit volume (MBq/ml). Image analysis was performed with VivoQuant software (inviCRO, Boston, US). Stroke volume was determined by thresholded segmentation of the high uptake area on the [^{99m}Tc]DTPA SPECT images and activity concentration ratio of the injured and intact hemispheres were calculated.

Data analysis and statistics

Of the 62 mice used in the MCAO experiments, 14 died before reaching the experimental endpoint and were therefore excluded from the analysis. Data analysis followed previously established protocols of our research group[29, 81, 86, 87]. For survival experiments with MCAO, mice were coded independently and randomized. Three investigators who were blinded to the analysis performed the surgeries, neuroscoring, MRI imaging, and infarct size calculation. Volumetric data were used to calculate the ratio of left/ right brain hemispheres (L/R ratio) and hemispheric LV (%HLV). To correct for the lesion-expanding effect of tissue edema, the method validated by Gerriets et al[88] was used. Edema-corrected LV (LVc) for lesions measured on T2 sequences were compared to LV uncorrected for edema. The space-occupying effect of edema formation was expressed using the increase of total hemispheric volume (%HSE).

Multiphoton image stacks were processed offline. Image stacks were auto leveled, background subtracted and converted to RGB color in Fiji. Movement artifacts were corrected using the "Template Matching" plugin in Fiji. The SD associated and subsequent intracellular calcium changes were measured on green fluorescent images (ΔF/F) by placing 4–10 m regions of interests (ROI) on the soma of selected astrocytes. Cells expressing both Ca^{2+} waves and subsequent Ca^{2+} oscillations were considered for comprehensive analysis. Arterioles were identified by their pial latero-medial anatomical branching. Arterioles and venules were differentiated with the help of 3D reconstruction relying on a z-stack of two-photon images. The analyzed penetrating arterioles and first order arterioles were direct branches of the pial arterioles. In addition, venules could be reliably discriminated from arterioles on the basis of their irresponsiveness to SD[81]. Additional, specific criteria to include a vessel into the analysis were as follows: (i) The intracellular Ca^{2+} wave of SD must have propagated fully over the astrocytes next to the vessel; (ii) The baseline diameter of penetrating arterioles was above µ5 m in order to have reliable assessment of vasoconstriction with respect to pixel size (i.e., 1 µm); and (iii) The penetrating arteriole optimally appeared in cross sectional view. Vascular diameters were either measured manually at baseline (i.e., prior to SD), maximum constriction, subsequent maximum dilation, and recovery or using the" Diameter" plugin in Fiji[89]. Recordings formed the subject of analysis in case vascular diameter alterations occurred in the presence of astrocyte Ca^{2+} waves.

Data are presented as mean±stdev, with individual data points overlaid in several graphs. The statistical analysis was conducted using SigmaPlot 12.5 (Systat Software, Inc.). The normality of data distribution was assessed using the Shapiro-Wilk test. Data sets with discrete values were analyzed using the Mann-Whitney test. For data sets showing a normal distribution, one-way ANOVA, two-way ANOVA, or repeated-measures ANOVA was applied, depending on the variables. ANOVA analyses were followed by Sidak-Holm's post hoc test. Statistical significance was set at $p<0.05$* and $p<0.01$**. The specific statistical tests applied are indicated in each figure legend.

RESULTS

Non-synchronized astrocyte Ca^{2+} oscillations follow the concurrent Ca^{2+} wave of spreading depolarization

Astrocyte Ca^{2+} waves are considered reliable indicators of astrocyte activation[90, 91], and astrocytic Ca^{2+} transients contribute to the regulation of several intracellular signaling cascades. Spreading depolarizations cause vast changes in intra- and extracellular ion concentrations and initiate among my others, changes in Ca^{2+} levels. Based on this, we selected a fluorescent calcium indicator dye to visualize intracellular Ca^{2+} dynamics during SDs, using multiphoton microscopy to record changes in fluorescence intensity in vivo.

Following the topical application of 1 M KCl on the brain surface, SD occurrence was confirmed by (i) the typical 77.5 ± 25.2 μm/s propagation velocity of the astrocyte Ca^{2+} wave [92], and (ii) the characteristic cerebrocortical microvascular changes associated with SD[81]. The typical intracellular fast astrocyte Ca^{2+} changes associated with SD have a fast propagation speed of 77.5 ± 25.2 μm/s), therefore the peak fluorescence maximum corresponding to the temporary steep elevation of Ca^{2+} appeared temporally synchronized in cells (Fig. $9A_2$,B). The Ca^{2+} wave was also temporally coincident with the SD-related arteriolar constriction (Fig. $9A_2$,B). Interestingly, the at a 183.64 ± 89.21 s delay with respect to the synchronized Ca^{2+} wave, the same astrocyte network showed non-synchronized Ca^{2+} oscillations (Fig. $9A_{4\text{-}6}$,B). These oscillations were of three times higher frequency (0.66 ± 0.32 event/minute/cell) when compared to spontaneous basal Ca^{2+} activity (0.19 ± 0.032 event/minute/cell). The oscillations in individual cells were random and repetitive. Temporal coincidence of the Ca^{2+} spikes between cells were not observed, but the typical pattern of Ca^{2+} oscillations occurred in association with the plateau of the SD-related arteriolar dilation (Fig. 9B). The peak fluorescence maximum of Ca^{2+} oscillations was smaller compared to the maximum amplitude of the prior Ca^{2+} wave in the same cells (54.02 ± 22.65 vs. 98.06 ± 24.35 ΔF/F, Ca^{2+} oscillation vs. Ca^{2+} wave) (Fig. 9C). Additionally, fewer astrocytes were involved in Ca^{2+} oscillations at a given time point, in contrast with Ca^{2+} waves, which engaged all astrocytes in the field of view virtually simultaneously (Fig. 9D).

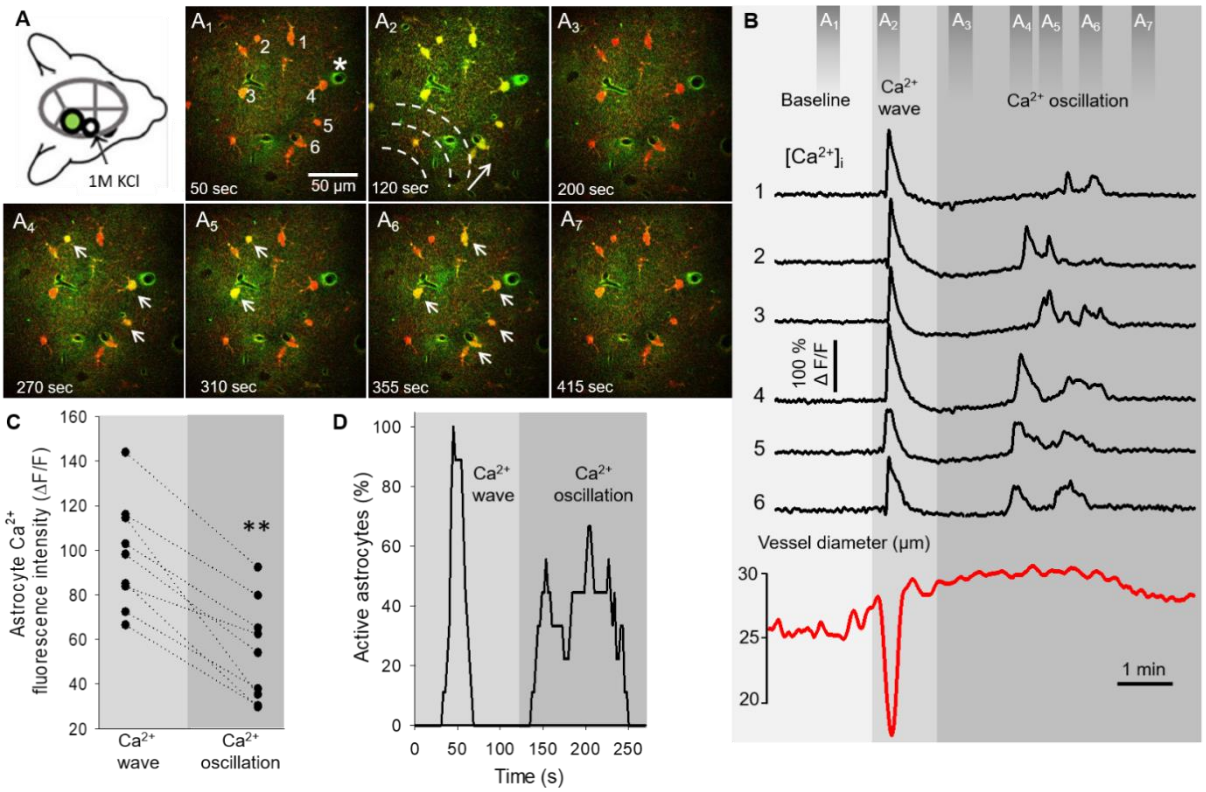

Figure 9. Astrocyte Ca^{2+} dynamics during spreading depolarization (SD) in the mouse somatosensory cortex. **A,** Schematic illustration of the closed cranial window preparation indicates the position of the imaging site (green). SD events were triggered by topical application of KCl in a smaller rostral open craniotomy (open circle). Images **A**$_{1–7}$ demonstrate astrocyte Ca^{2+} changes (Fluo-4 AM, green) associated with SD. Astrocytes (numbered 1–6 on A1) were selectively labelled by SR101 (red). Dashed lines and arrow **A**$_2$ denote the direction of SD propagation; white arrows are pointing at astrocyte somata displaying Ca^{2+} oscillations **A**$_{4–6}$. **B,** Astrocyte Ca^{2+} changes (i.e., wave and oscillations) extracted from regions of interests (numbered 1–6 in **A**$_1$) coincide with arteriole diameter changes (labelled with * in **A**$_1$) during SD. Dark grey bars (top) indicate time points of the corresponding images (**A**$_{1–7}$). **C,** Ladder plot shows the peak fluorescence maximum (ΔF/F) of Ca^{2+} waves and subsequent oscillations derived from nine cells. **D,** Percentage of astrocytes (n = 9 in total) displaying Ca^{2+} changes at each time point during acquisition. Ca^{2+} events were defined as $\Delta F/F \geq 13\%$ with respect to baseline fluorescence. Images were taken at a cortical depth of 55–75 µm. Data are given as mean ± st.dev. Two-tailed paired t-test was used for statistical analysis with the level of significance set at $p<0.01$**.

TFP enhances the cerebral blood flow response to SD in the non-ischemic mouse cortex

Following confirmation of astrocyte activation during SDs, we hypothesized that the elevation of intracellular Ca^{2+} may activate regulatory pathways dependent on Ca^{2+} sensitive calmodulin. Based on this, we proceeded to investigate the effects of CaM inhibitor TFP on elicited depolarizations and concomitant vascular responses. DS commonly occur in AIS and reflect the excitability of brain tissue. Furthermore, the magnitude of the CBF response to SD reflects the state of vascular reactivity.

These experiments were conducted in non-ischemic brains. Since the first SD appearing after the onset of ischemic stroke has substantially different properties regarding both changes of LFP and CBF, it was analyzed separately. Both the frequency of KCl-induced SDs and their relative amplitude tended to be reduced by TFP (e.g., amplitude of the first SD in a train:

12.96±7.05 vs. 18.88±2.64 mV, TFP vs. control), although the reduction did not reach statistical significance (Fig. 10A-C). TFP had no effect on the CBF response to the first SD in a train (peak: 118.9±22.7 vs. 112.7±23.5 %, TFP vs. control). However, the amplitude of subsequent recurrent SDs exceeded baseline CBF levels in the TFP group (122.6±23.5 %), whereas it remained below baseline in controls (93.6±26.7 %) (Fig. 10D-E). This difference was remarkable for the area under the curve (AUC) of the hyperemic phase of the CBF response associated with recurrent SDs (9419.4±2173.6 vs. 5444.7±1828.2 %×s; TFP vs. control) (Fig. 10F).

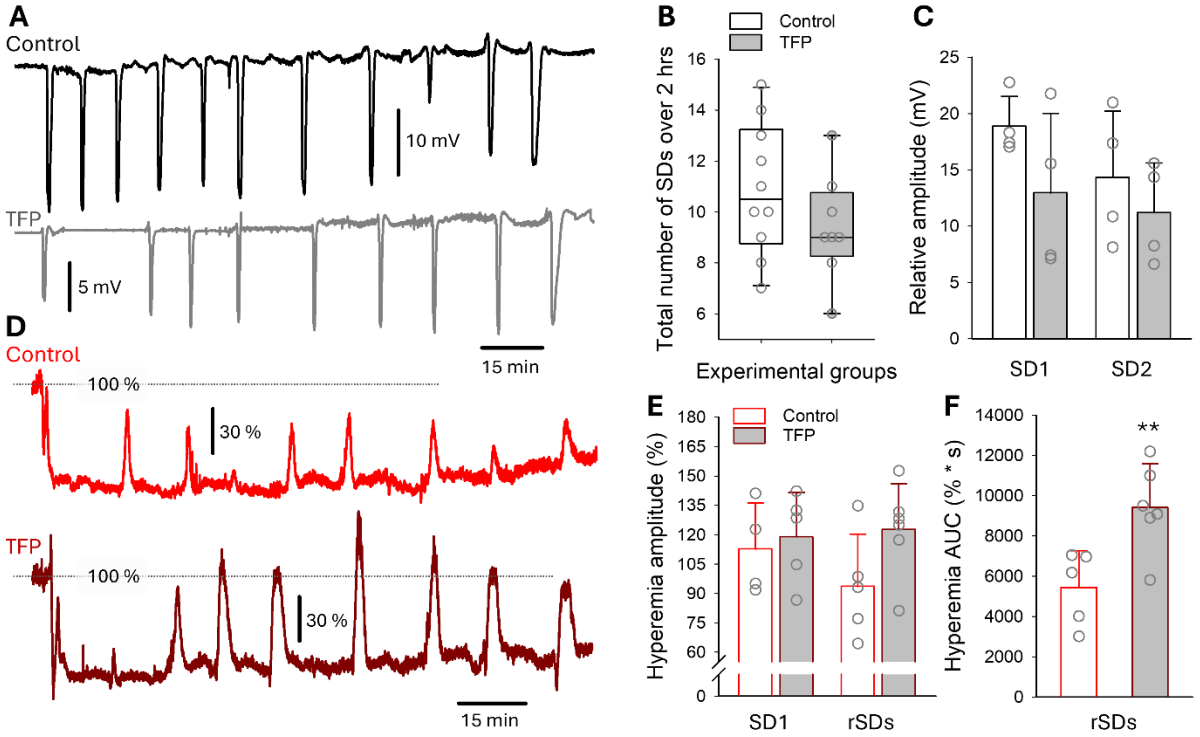

Figure 10. Treatment with trifluoperazine (TFP) augments hyperemia coupled with spreading depolarization (SD). **A,** Representative direct current (DC) potential recordings from a control (upper trace) and a TFP-treated preparation (lower trace) illustrate the pattern of recurrent SDs triggered by continuous exposure to topical KCl. **B-C,** Both the total number of SDs and the relative amplitude of the first (SD1) and second (SD2) events tended to be lower in the presence of TFP, although the differences did not reach statistical significance. **D,** Representative laser-Doppler flowmetry traces from a control (upper trace) and a TFP-treated preparation (lower trace) show the kinetics of the SD-coupled cerebral blood flow (CBF) response. **E-F,** The amplitude of hyperemia associated with recurrent SDs (rSDs) showed a tendency to increase in the TFP group, with a significantly greater area under the curve (AUC). Data sets with discrete values (B) are presented as a box plot with individual data points overlaid and were analyzed using the Mann-Whitney test. The normality of data distribution was confirmed with the Shapiro–Wilk test (C, E, F), and normally distributed data are shown as mean±stdev with individual data points overlaid. One-way ANOVA was applied for statistical analysis. Statistical significance was set at $p<0.01$** (TFP vs. control).
TFP: trifluoperazine, SD: spreading depolarization, rSD: recurrent spreading depolarization, AUC: area under the curve

Transient MCAO creates perfusion deficit and ischemic lesion formation, as verified by laser Doppler and MRI imaging

Following experiments carried out in intact brains, we carried on by introducing an animal model of acute ischemic stroke for further investigations. Our AIS model had a mortality rate of 25%, which is consistent with earlier data from the relevant literature reporting mortality rates of up to 50% following MCAO in mice[93]. Successful occlusion of the middle cerebral artery by MCAO was confirmed by measuring CBF with a laser Doppler probe placed over the parietal cortex (Fig. 11A). Perfusion in the area supplied by the MCA dropped to levels characteristic of the ischemic core (13.11±6.00%) and was further reduced by the appearance of a spontaneous SD (2.95±1.35% mean lowest perfusion) (Fig. 11B). Although filament removal resulted in complete recanalisation, prolonged oligemia was observed following reperfusion (Fig. 11B), which is characteristic following ischemia induced SDs[30, 94].

Before initiating pharmacological treatments, ischemic lesion formation was verified by MRI imaging 72 hours after MCAO. The lesion volumes (LVs) ranged between 17-130 mm^3, corresponding to a relative size of 7.31-54.17% of the total left cerebral hemisphere (hemispheric lesion volume, HLV%; 35.71±12.06%). The regions of T2-weighted hyperintensity were consistently accompanied by areas of restricted diffusion, as measured in ADC maps (5.01±0.32 x 10^{-4} vs. 7.89±0.60 x 10^{-4} mm^2/sec; lesioned vs. intact hemisphere). This confirmed the development of the lesion. The volumes of the areas with decreased ADC were always within the T2 lesion area and ranged between 3.0-115.6 mm^3 and were smaller than the adherent LV (range between 1.29-46.55 HLV%; mean±stdev 23.87±11.94 HLV%).

Progression of cerebral edema compromises lesion volume estimation

Cerebral edema progression significantly affected the accurate estimation of hemispheric LVs. Differences in total hemispheric volumes were observed due to brain swelling, as indicated by the left-right hemispheric ratio (L/R ratio), which ranged between 102.2-165.4 %; with a mean of 121.90 ± 16.94 % (Fig. 11C). The increase in volume of the left hemisphere distorted the estimation of LVs (R=0.724, p=0.0023). The space-occupying effect of brain edema was quantified by calculating the increase in volume of the affected hemisphere (%HSE). %HSE is a numerical expression of the measured L/R ratio values, displaying linear relationship between the two values (R=0.997, p=0.009). The swollen tissue within and around the lesion linearly increased the volume of the affected hemisphere by 17.32±12.39% and enlarged the LVs (R=0.705, p=0.003) (Fig. 11D).

To accurately characterize the lesions, we corrected the LVs for edema (LVc) using a previously described formula[88]. The application of edema correction resulted in a significant decrease in LVs (44.36±23.56 vs. 87.13±30.64 mm^3; LVc vs. LV) (Fig. 11E).

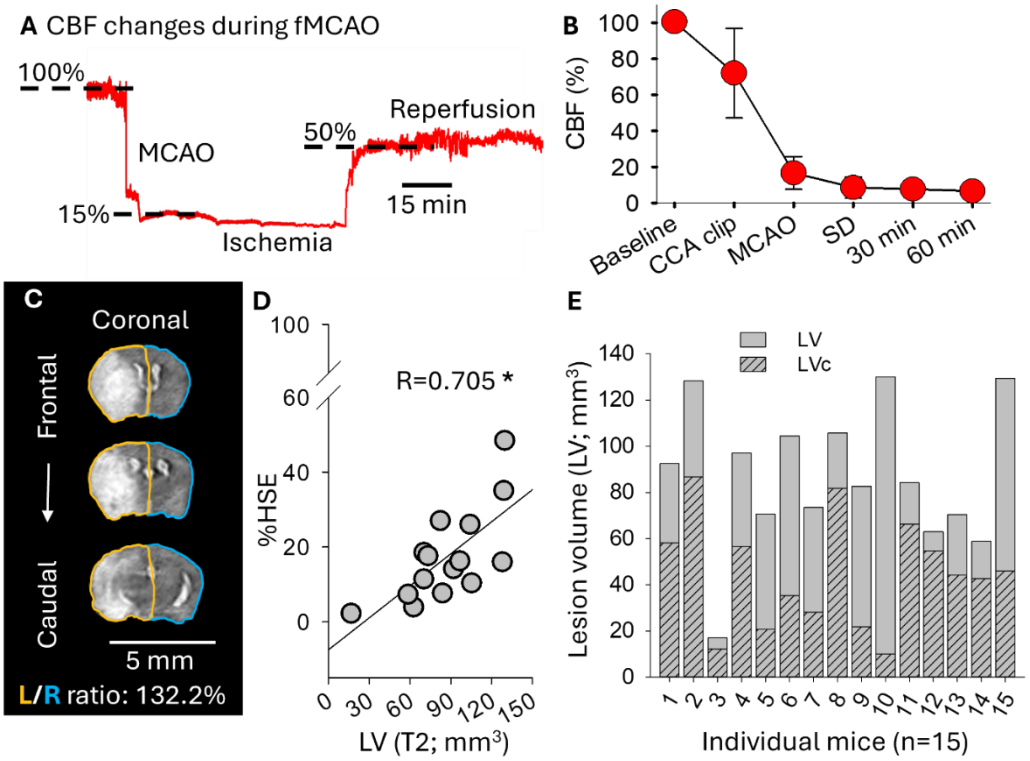

Figure 11. Verification of ischemic CBF conditions and formation of ischemic lesion following transient MCAO. Correcting for edema in MRI images more accurately estimates lesion volume. **A,** Representative recording of CBF changes during fMCAO measured by a laser Doppler probe placed over the parietal cerebral cortex of the mouse. **B,** CBF in the cortical area supplied by the MCA drops to levels characteristic of the ischemic core during fMCAO. **C,** The left/right hemispheric ratio (L/R ratio) was used to estimate the swelling of the left hemisphere affected by acute ischemic stroke (AIS). Note the shift of the midline and the expansion of the left hemisphere (outlined in yellow). **D,** Tissue swelling or edema (increase in hemispheric volume due to space-occupying edema, %HSE) shows a linear relationship with lesion volume (LV) on T2 weighted MRI images (linear regression: R=0.705, p=0.003, p<0.05*). **E,** Edema correction provides better estimation of true lesion volume (corrected lesion volume, LVc).

Lesion volumes display no relationship with somatosensory deficits

In addition to lesion size, we planned to evaluate sensorimotor function as an outcome following AIS. In the clinical setting, routine assessment of neurological deficits is often predictive in AIS patients, helping clinicians to confidently estimate the extent and location of lesions[95, 96]. Furthermore, the severity of symptoms correlates well with lesion size estimated through neuroimaging[97]. Over the past two decades, preclinical rodent models of AIS have often assumed a positive correlation between lesion size and neurological deficit, just like in human patients[98]. However, the data are contradictory, since some studies state that neurological deficits are not necessarily related to lesion size in rodent stroke models[26]. To resolve this

discrepancy, we decided to investigate the relationship between sensorimotor deficit and lesion volume in our own dataset.

The GNS score ranged from 7 to 15 at 72 hours of survival. Interestingly, no correlation was observed between LVs and GNS, either before or after edema correction (LVc) at the time of MRI (R=0.0581, p=0.837 and R=0.167, p=0.552; LVc and LV). The lack of correlation between the T2-weighted LVc and the GNS points at 24 (R=0.170, p=0.545), 48 (R=0.0808, p=0.775), or 72 hours of survival of the 15 mice (as shown above) confirms that the LVcs do not predict neurological outcome (Fig. 12C&D). Furthermore, the volume of decreased ADC within T2 lesions did not correspond to the GNS score (R=0.392, p=0.149), indicating that the GNS score is not a reliable indicator of ADC volume. However, the GNS score measured at 24 hours strongly correlated with the GNS score at 72 hours of survival of the same animal (R=0.748, p=0.0013). Therefore, neurological deficits assessed at 24 hours of survival proved to be predictive of the GNS score at later time points.

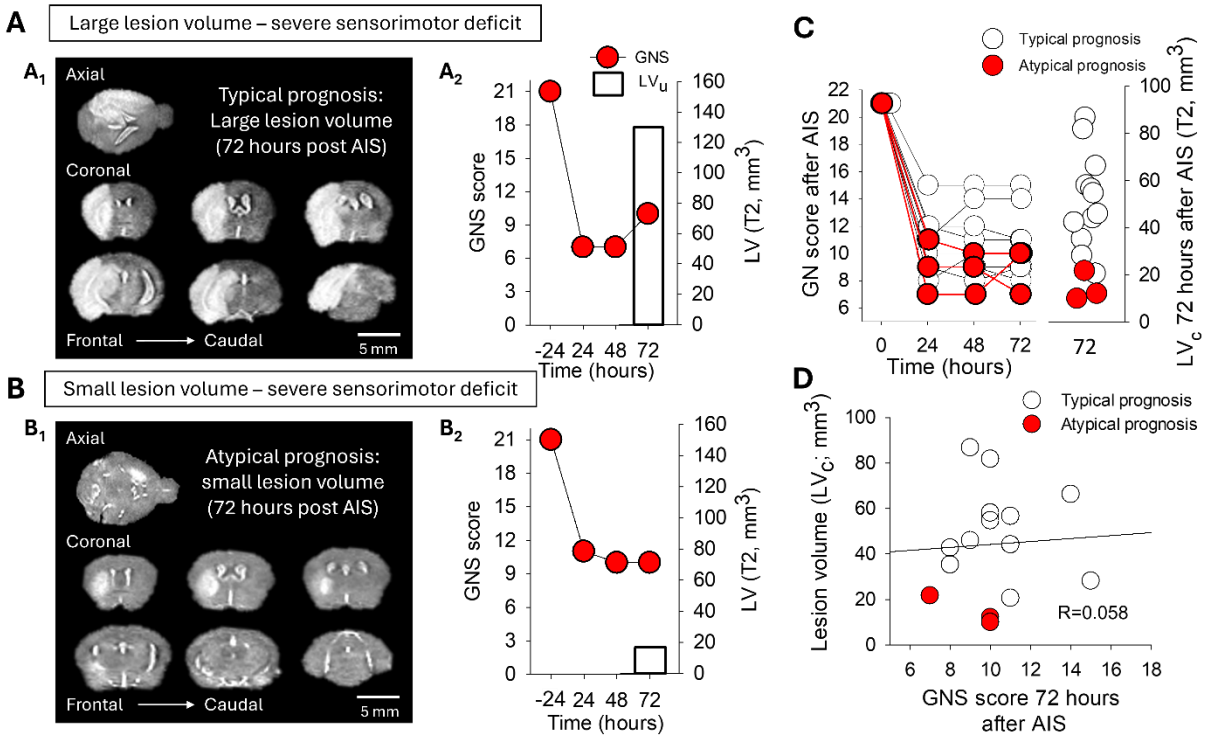

Figure 12. A subgroup of mice exhibits a paradoxical relationship between small lesion volume and severe neurological deficit. **A,** A representative mouse with a typical prognosis displays low Garcia Neuroscore Scale (GNS) score over the course of 72 hours of survival (A_2), and a large lesion volume as measured on the T2-weighted MRI sequence (A_1). **B,** A mouse with severe neurological deficit (B_2) was identified with a poor prognosis and small T2 lesion volume (B_1). **C,** GNS score assessed every 24 hours after AIS induction and corrected lesion volume (LVc) on day 3 are unrelated. **D,** There was no linear relationship between lesion volume and GNS score assessed 72 hours after AIS (linear regression: R=0.058, p=0.837).

Paradoxical association of small lesion volume with severe neurological impairment

Three of the 15 mice evaluated exhibited a paradoxical relationship between LVs and neurological deficits, identified as “atypical prognoses” (Fig. 12C). These animals showed lower LVc compared to the rest of the mice (14.64 ± 6.25 vs. 51.79 ± 19.96 mm^3, atypical vs. typical prognosis) but still showed severe residual deficits (GNS score at 72h: 9 ± 2 vs. 11 ± 2; atypical vs. typical prognosis) (Fig. 12C). MRI and GNS data for one mouse with an atypical prognosis are presented in Figure $12B_{1\text{-}2}$. Despite the presence of a mild lesion, severe neurological deficit was observed. In contrast, the T2-weighted LVs were compatible with the measured neurological deficit in 12 out of 15 mice, identified as having a “typical prognosis”. For instance, the mouse presented in Figure $12A_{1\text{-}2}$ showed a typical prognosis due to the severe LV on the T2-weighted MRI sequences, which was accompanied by a severe neurological deficit represented by the low GNS score. The linear relationship between LVc and the GNS score weakened by day 3 of survival (R=0.146, p=0.61 vs. R=0.485, p=0.110; 72 vs. 24 h) in the group of animals with typical prognosis. This finding suggests that the paradoxical relationship of the parameters is not caused by atypical cases. Finally, as expected, the corrected lesion volumes displayed no relationship with the GNS scores measured 72 hours after AIS (R=0.058, p=0.837). Importantly, the exclusion of "atypical cases" (n=3 animals) had no significant effect on the data (R=0.298, p=0.92), as there was still no linear relationship between GNS scores and lesion volume in "typical cases".

Since severe edema formation accompanied the ischemic lesion, the relationship of brain swelling and functional deficit was also investigated. The association between the calculated %HSE and the GNS scores at 72 hours of survival was not significant (R=0.235, p=0.398). This suggests that the neurological deficit associated with AIS is not solely attributed either to the progression of edema.

TFP treatment decreases lesion size irrespective of edema formation

Magnetic resonance imaging (MRI) performed 3 days after MCAO revealed distinct focal cortical and striatal infarcts in all experimental groups (Fig. 13A), as indicated by an increased T2 signal with concurrent restricted diffusion in the affected area. TFP was administered in two treatment regimens. Both dosage protocols were well tolerated and reduced lesion volumes; however, only the higher single dose of TFP administered upon recanalization resulted in a significant reduction in lesion size compared to the control group (52.51±15.56 vs. 31.98±14.46 vs. 20.51±15.61 mm^3, control vs. TFP1 vs. TFP5) (Fig. 13B). As TFP was expected to hinder

tissue swelling, the space-occupying effect of edema concomitant to ischemia was measured as the increase in hemispheric volume (%HSE). However, there was no difference in extent between the groups (20.91± 14.91% vs. 25.35± 5.74% vs. 21.07± 6.33%, control vs. TFP1 vs. TFP5) (Fig. 13C), suggesting that even smaller lesion volumes were accompanied by severe tissue swelling.

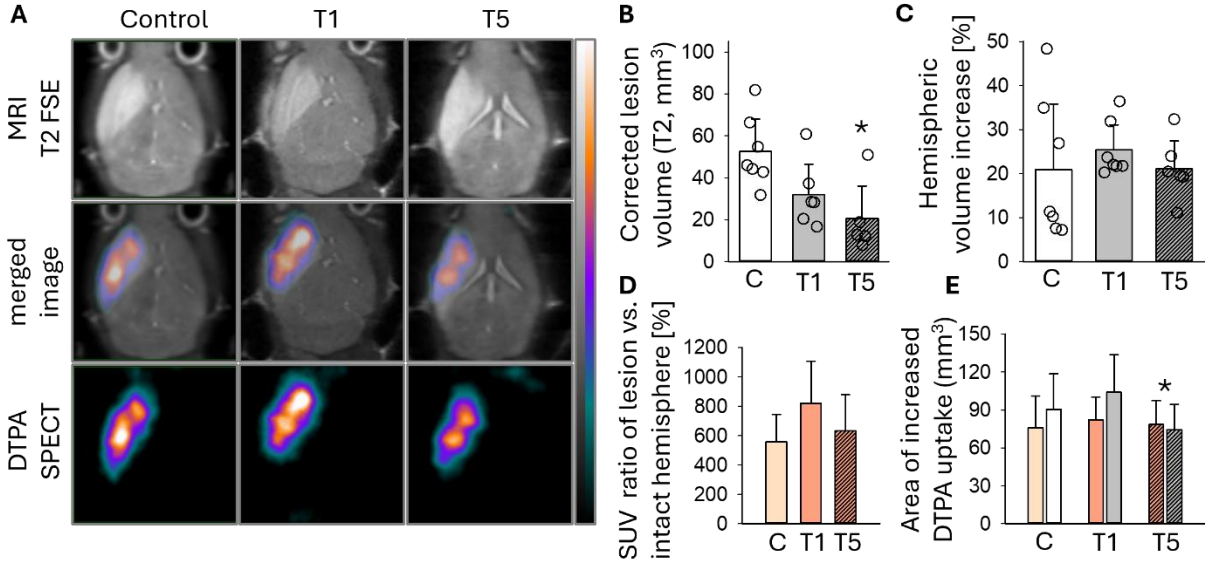

Figure 13. Single dose of TFP decreases lesion size but does not alter the degree of ischemia-associated brain edema or the extent of blood-brain barrier (BBB) injury in the subacut phase of ischemic stroke. **A,** Representative images of MRI T2 FSE measurements and SPECT maps of increased DTPA uptake from the same animals. Scales on the right side represent the color-coding of intensity. **B,** Lesion volumes corrected to the space-occupying effect of edema proved to be smaller in animals treated with a single, higher dose of TFP upon recanalization (One-Way ANOVA, p=0.02). **C,** Average increase in hemispheric volume due to lesion expanding effect of edema is unaltered in the treated groups (One-Way ANOVA, p=0.535). **D,** Standardized uptake value (SUV) describing the activity concentration of the radiopharmacon DTPA used in SPECT experiments, was higher in the stroke-affected areas compared to the opposite, healthy hemisphere, indicating severe BBB leakage. Intact hemisphere values were used as the 100% baseline. No difference between the experimental groups was observed (One-Way ANOVA, p=0.126). **E,** The brain volume of increased DTPA uptake indicating BBB injury is similar in all groups (orange bars). However, the ratio of the volumes of increased enhancement in SPECT and the corresponding lesion size measured on MRI T2 sequences (grey bars) is increased in the T5 group (One-Way ANOVA, p=0.02). BBB: Blood-brain barrier, SUV: Standardized uptake value, TFP1 or T1: TPF administered as 1 mg/kg every 24 with the first dose upon recanalisaton, TFP5 or T5: TPF administered as a single dose of 5 mg/kg upon recanalization, C: control.

SPECT scans were performed right after MRI acquisitions to assess blood-brain barrier (BBB) permeability (Fig. 13A). Under physiological conditions, the radiolabeled compound DTPA does not cross the BBB therefore its presence in the brain parenchyma is minimal. However, in ischemic stroke, the affected brain tissue often undergoes BBB disruption, resulting in extravasation of DTPA. Consequently, regions displaying elevated DTPA uptake following a stroke are likely to correspond to areas of BBB breakdown, enabling the formation of vasogenic edema. Increased DTPA uptake was detected in areas affected by stroke compared with adjacent areas in the ipsilateral left hemisphere and the intact right hemisphere (Fig. 13A). No significant

differences in SUV activity were found between the control and treated groups (558.00±185.78% vs. 820.86±285.66% vs. 632.33±247.14%, control vs. TFP vs. TFP5; one-way ANOVA, p=0.126) (Fig. 13D), nor in the overall area of elevated isotope accumulation (75.74±25.16 vas. 82.14±17.95 vs. 78.59±18.81 mm^3, control vs. TFP vs. TFP5; one-way ANOVA, p=0.846) (Fig. 13E). However, the volume of increased DTPA uptake relative to the lesion volume, as measured using the T2 FSE MRI sequence, was greater in the TFP5 animals than in both the control and TFP1 groups (ratio of 0.84±0.13% vs. 0.81±0.10% vs. 1.07±0.14%; control vs. TFP1 vs. TFP5; one-way ANOVA, p=<0.05) (Fig. 13E). This suggests that regions with elevated uptake may even extend beyond the borders of lesions detected using MRI imaging.

TFP treatment improves neurovascular coupling and attenuates neurological deficits

As TFP treatment was found not to reduce the extent of tissue swelling and previously, we observed improved vascular reactions to elicited SDs, we decided to explore other possible causes of the milder lesion volume.

Neurovascular coupling (NVC) is a fundamental physiological mechanism that ensures the constant delivery of the oxygen and nutrients required for proper neuronal function. This mechanism is based on the neurovascular unit, a complex system of connections between astrocyte endfeet, neurons and endothelial cells. Neural activation results in an increase in local CBF, known as functional hyperemia. However, ischemia damages the NVU and impairs CBF responses, serving as a marker of ischemic injury. Whisker-pad stimulation is a well-established method of testing NVC, so it was chosen to test the effectiveness of neurovascular coupling three days after MCAO. The mechanical stimulation of the whisker-pad evokes neural activation and consequent functional hyperemia in the contralateral barrel cortex, which can be measured with probes placed over the parietal bone.

An increase in local field potential (LFP) activity was used to verify neuronal activation in response to contralateral whisker stimulation. The functional hyperemia evoked by stimulation was diminished in the middle cerebral artery territory of the stroke-affected hemisphere compared to the intact, contralateral cortical region (4.01±3.77% vs. 22.39±9.48%; control MCAO vs. control intact cortex) (Fig. 14A&B). TFP treatment significantly improved hyperemia amplitude compared to the control group, independently of the treatment regimen. Furthermore, CBF responses were comparable to those of the intact cortex (4.01 ± 3.77% vs.

20.65 ± 8.80% vs. 19.49 ± 11.93% vs. 22.39 ± 9.48%; control MCAO vs. TFP1 MCAO vs. TFP5 MCAO vs. TFP intact cortex) (Fig. 14B).

Although all mice were equally impaired 24 hours after MCAO, as reflected by GNS values averaging 9-10 (with 21 indicating normal performance), animals that received treatment were found to perform better in functional tests on the second and third post-operative days, regardless of the treatment protocol, with group averages increasing to 12-13 points compared with 10-11 points in the control group (Fig. 14C).

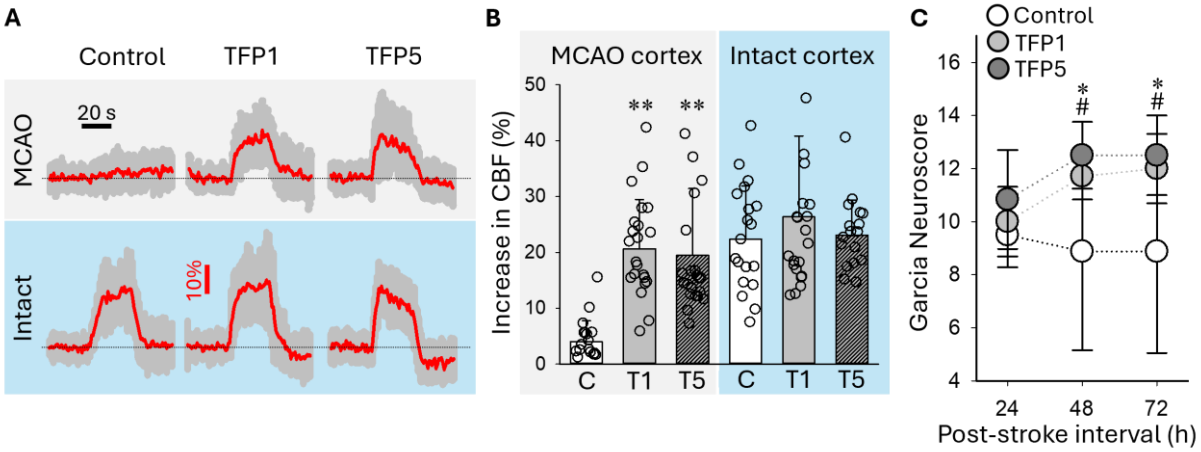

Figure 14. TFP treatment improves both functional hyperemia in response to whisker-pad stimulation and functional outcome in the subacute phase following MCAO. **A,** Averaged curves of functional hyperemia in response to contralateral whiskerpad stimulation. The dotted line marks the baseline CBF right before stimulation onset, which is taken as the reference value of 100%. **B,** TFP restores the amplitude of functional hyperemia to levels comparable with those of an intact hemisphere, regardless of the treatment regimen (One-Way ANOVA, $p<0.001$). **C,** Sensorimotor function is improved at 48 and 72 hours post-MCAO in both TFP treatment groups compared to the control animals (Two-Way ANOVA, $p<0.001$).
MCAO: Middle cerebral artery occlusion, TFP1 or T1: TPF administered as 1 mg/kg every 24 with the first dose upon recanalisation, TFP5 or T5: TPF administered as a single dose of 5 mg/kg upon recanalisation, C: control, CBF: Cerebral Blood Flow.

DISCUSSION

The aim of our work was to determine whether limiting early edema formation after ischemic stroke could reduce infarct size and improve sensorimotor outcomes. To address this question, we pharmacologically targeted a Ca^{2+}-dependent signaling pathway in astrocytes that regulates the intracellular trafficking of aquaporin-4, the principal mediator of water permeability in the brain.

In the first phase of our experimental work, we visualized astrocyte Ca^{2+} changes associated with SD in the anesthetized mouse somatosensory cortex. Besides proving the transient elevation of intracellular Ca^{2+} levels concomitant to depolarizations, this is the first in vivo study to describe the delayed astrocyte Ca^{2+} oscillations following SD in vivo.

Astrocyte Ca^{2+} waves indicate glial activity in response to mechanical, electrical, or pharmacological stimulation, which propagate from cell-to-cell with a relatively slow velocity of 10–30 μm/s[99, 100]. Under pathological conditions like seizures or SD, the propagation velocity within the astrocyte network increase, and astrocytes display much faster Ca^{2+} waves (50-80 μm/s)[92, 101]. The Ca^{2+} waves measured in our model were typical of SD because they propagated at a speed of 77.5 ± 25.2 μm/s, delineating the direction of SD propagation (Fig. 9). Additionally, the arteriolar constrictions coupled with the Ca^{2+} waves stood in good agreement with earlier reports, and confirmed SD occurrence in our model[92].

Examining the duration of the SD related Ca^{2+} events in individual astrocytes, we discriminated short (≤33 s) and long (>33 s) astrocyte Ca^{2+} waves during SD. A long Ca^{2+} wave was captured in one experiment, in which the SD-related Ca^{2+} elevation spatially radiated from a single astrocyte (Fig. 9).

We confirmed the occurrence of delayed random Ca^{2+} oscillations in astrocytes 2–4 min after the passage of the SD-related Ca^{2+} wave, occurring at a frequency of 0.66 ± 0.32 events/min/cell (0.01 Hz) in a chosen astrocyte soma. In agreement with the slice results of Wu et al.[102], we observed that the frequency of these post-SD oscillations was three times higher than the spontaneous Ca^{2+} fluctuation of astrocytes during baseline (0.19 event/min/cell)[102]. Although the propagation of these spontaneous Ca^{2+} oscillations in cell cultures and brain slices was shown in an earlier study[103, 104], we did not discern synchronization of the Ca^{2+} oscillations among the cells[104]. The cell-to-cell propagation of the oscillations could have escaped detection in our preparations in case the astrocyte linked to the oscillating cell fell out of the plane of

view, or if the velocity of cell-to-cell propagation of the signal was too rapid with respect to the recording's sampling frequency. Astrocyte Ca^{2+} oscillations had a smaller fluorescent peak amplitude when compared to the prior Ca^{2+} waves, which could be due to different mechanisms in the background of these two events. For instance, antagonism of $GABA_B$ receptors, depletion of intracellular Ca^{2+} stores, or blockade of IP3 receptors all attenuated the Ca^{2+} oscillations, but had no significant effect on the SD-related Ca^{2+} wave[102, 104]. One could therefore speculate that while Ca^{2+} waves rely on multiple pathways mobilizing external Ca^{2+}, post-SD oscillations are largely dependent on Ca^{2+} release from the endoplasmic reticulum or mitochondria.

Among the various channels contributing to elevations in intracellular Ca^{2+} levels, one of the principal routes of Ca^{2+} entry activated during SDs is through Transient Receptor Potential Vanilloid 4 (TRPV4) channels. TRPV4 channels are non-selective cation channels with substantial Ca^{2+} conductance and are abundantly expressed in astrocytes, particularly in astrocytic endfeet, where they form a functional complex with AQP4 channels[105]. During SDs, TRPV4 channels contribute significantly to calcium transients in both astrocytes and neurons[106].

TRPV4 and AQP4 act cooperatively to regulate water and ion homeostasis. Studies using knockout mouse models demonstrate that deletion of either channel disrupts the function of the other, indicating a strong functional interdependence[107, 108]. Further evidence suggests that Ca^{2+}-dependent intracellular trafficking of AQP4 is initiated by Ca^{2+} influx through TRPV4 channels[75]. In this process, Ca^{2+} stabilizes the interaction between AQP4 and calmodulin (CaM), the key mediator driving AQP4 translocation.

As our experiments demonstrated the presence of dynamic intracellular Ca^{2+} changes induced by SDs that are capable of stimulating AQP4 translocation in astrocytes, we next investigated the effects of pharmacological interventions targeting this Ca^{2+}-sensitive signaling pathway.

In our second set of experiments, we set out to explore whether administration of TFP, a calmodulin inhibitor that was previously shown to block AQP4 translocation to the astrocytic plasma membrane[67, 75], could inhibit cytotoxic edema formation during the early phase of AIS, limit infarct maturation, and improve the recovery of neurological and cerebrovascular function.

We selected TFP based on several key considerations. Experimental and genetic studies have demonstrated that AQP4 plays a phase-dependent, dual role in ischemic stroke pathology: it is critically involved in the development of cerebral edema during the acute phase, while also

facilitating water clearance during vasogenic edema and contributing to interstitial fluid drainage via glymphatic pathways[54]. In accordance with that, permanent inhibition of AQP4 during the acute phase has been shown to reduce edema formation[109, 110]. However, while studies using AQP4 knockout mice also reported a marked reduction in early cytotoxic edema following focal cerebral ischemia, they also described increased hemispherical swelling three days after MCAO, despite improved functional outcome and reduced lesion size[70]. Because prolonged AQP4 deletion or sustained inhibition may impair edema resolution and potentially exacerbate infarct expansion at later stages, the therapeutic value of targeting AQP4 is critically dependent on timing. In this context, TFP represents a promising candidate, as it transiently alters the cellular localization of AQP4 without directly inhibiting its function. Our therapeutic approach in AIS mice was designed to offer translational relevance, as TFP was delivered as a post-treatment, with administration initiated after recanalization. Moreover, TFP administration was targeted to the hyperacute phase, when cytotoxic edema formation is prominent and the risk of interfering with later edema resolution is minimal. Finally, the post-recanalization application of TFP is reversible, as inhibition of AQP4 translocation is lifted once the drug is cleared, thereby allowing AQP4-mediated edema resolution at later time points. Finally, because TFP is a commercially available drug approved for psychiatric use, it represents a feasible candidate for clinical translation through drug repurposing.

In contrast to the expectations, neither bolus nor repeated TFP treatment following MCAO resulted in a reduction of edema size as assessed by MRI. Importantly, however, infarct volume was significantly reduced in line with recent evidence[77, 111] and neurological outcomes improved, particularly when TFP was administered as a bolus immediately after recanalization (Fig. 13&14). To resolve this discrepancy, we propose that while TFP exerts its effect on acute osmotic stress and cytotoxic edema[29] and therefore helps to limit early neuronal damage, MRI performed 3 days after MCAO reflected the additional, delayed vasogenic edema[53, 56]. This concept is reinforced by a study done on AQP4 knock out mice, where infarct size was reduced following MCAO without reduction in the concomitant cerebral edema[70]. Our theory is also underlined by data obtained from osmotically challenged acute brain slice preparations, used to gain mechanistic insight into the acute events within the first hour after the insult (Tóth et al., 2026, under review) (Fig. 15). These data demonstrated that tissue swelling and AQP4 immunolabeling are reduced in the presence of TFP. This interpretation is further supported by our findings showing that BBB leakage, assessed by SPECT, was not affected by TFP (Fig. 13). This appears to be in contrast to a previous report demonstrating BBB protection by TFP in

immortalized mouse brain microvascular endothelial cells under ischemic conditions[111]. Still, TFP was beneficial in protecting against neural injury, as evidenced by reduced infarct size after MCAO (Fig. 13). In addition, TFP promoted functional recovery as shown with the GNS test (Fig. 14). Taking these results together, we argue, in light of our additional cerebrovascular findings, that TFP exerts neuroprotective effects possibly by improving cerebrovascular function, either in addition to, or as a consequence of, counteracting astrocyte swelling.

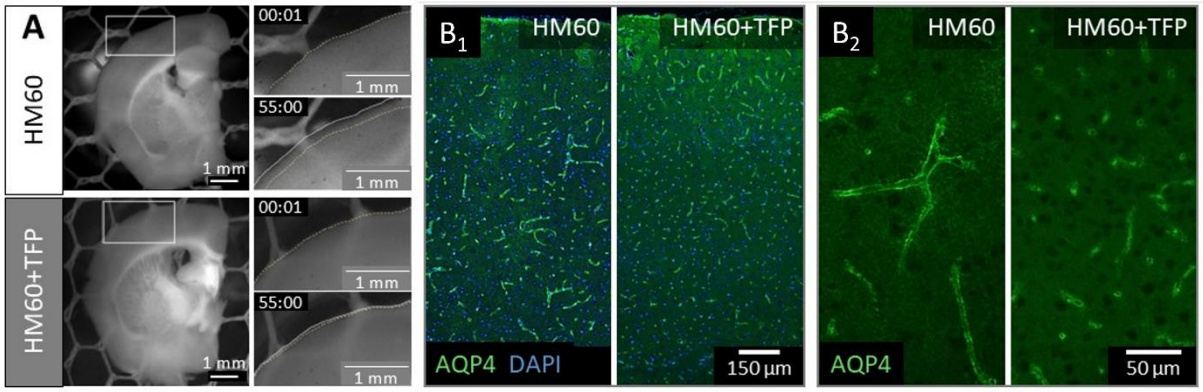

Figure 15. Representative cases from our ongoing work show that trifluoperazine (TFP) mitigates brain slice swelling and represses aquaporin-4 (AQP4) expression in osmotically challenged brain slice preparations. **A,** Representative intrinsic optical signal (IOS) images demonstrating brain slice swelling in hypoosmotic artificial cerebrospinal fluid (aCSF) with reduced NaCl concentration from 130 mM to 60 mM (HM60) alone or with the addition of TFP (HM60+TFP). Tissue swelling is indicated by the displacement of the contour of the parietotemporal cortex in each condition (insets). The time stamp is shown as min:sec. **B,** Fluorescent images immunostained for AQP4 showed reduced and more fragmented signal in TFP-treated slices.

Indeed, we found that TFP greatly improved neurovascular coupling in ischemic tissue after MCAO (Fig. 14), as well as the CBF response to SD in the optimally perfused cortex (Fig. 10). Previous studies using AQP4 inhibitor TGN-020 reported significantly increased regional cerebral blood flow in wild type mice but not in AQP4 knock-out animals, suggesting a relationship between hindered AQP4 function and increased cerebral circulation[112]. Astrocytes are intimately apposed to the microvascular wall, covering more than 95% of the vascular surface with their endfeet where AQP4 is abundantly expressed, and are essential regulators of vascular tone during neurovascular coupling with somatosensory stimulation[113]. Likewise, astrocytes play a pivotal role in shaping the CBF response to SD[39] and are heavily implicated in SD itself[114]. Adding further complexity, SD is accompanied by astrocytic swelling[115] and contributes to cytotoxic edema with the involvement of AQP4[43, 45]. Swelling of astrocytic endfeet compresses the microvasculature, occurring within an hour after acute brain injury, peaking around 6 hours post-impact, and gradually resolving by approximately day 3, as described in human samples[116]. This physical compression is understood to increase capillary transit time heterogeneity, which can critically reduce oxygen availability[116]. We suggest that targeting AQP4 and thus reducing astrocyte swelling with TFP may therefore contribute to the

observed improvement in cerebrovascular function by relieving the physical compression of cerebral vessels.

Alternatively, ischemia and cytotoxic edema may disrupt the neurochemical machinery underlying astrocytic vasoregulation. Astrocytes release both vasodilatory (prostaglandin E_2, PGE_2) and vasoconstrictive (20-hydroxyeicosatetraenoic acid, 20-HETE) metabolites of arachidonic acid in various contexts, with 20-HETE synthesis being markedly increased in association with increased microvascular tone in ischemic brain tissue and during SD[117-119]. Although no experimental evidence currently indicates that astrocytic cytotoxic edema directly drives increased 20-HETE synthesis, both AQP4 translocation to the plasma membrane and 20-HETE production are mechanistically linked to astrocytic Ca^{2+} oscillations that are augmented by ischemia[75, 118, 119]. It is therefore conceivable that TFP, in addition to its inhibition of AQP4 translocation and the resulting attenuation of swelling, suppresses astrocytic vasoconstrictor signaling or rescues vasodilator signaling, thereby shifting the balance toward decreased microvascular tone.

During the experimental work, in the MRI acquisitions assessed 3 days following we noticed in many cases pronounced hemispherical swelling on the side affected by MCAO. The development of ischemic lesions is always associated with cerebral edema, and this unavoidable phenomenon is well studied not only in animal models, but also in stroke patients. The swelling is more pronounced in patients with successful recanalization because the restoration of active blood flow is accompanied by ion and water entry through the damaged capillary walls into the brain[120]. The development of brain edema typically peaks on day 3-4 and has been shown to increase the mortality rate of MCA territory strokes by 80%, as the initial swelling progresses to space-occupying edema[121]. The most severe form of brain edema following AIS involving the entire MCA territory is called malignant MCA infarction, which is known to have devastating effects on patients because of the compression of surrounding tissue, possible herniation, and death in one-fifth of patients within the first week[122]. Cerebral edema is now the subject of intense research in animal models[29, 123]. Since focal brain edema exerts compression on the surrounding tissue and expands the size of the lesion, the volume of edema, and the volume of the edema-free infarcted regions can be calculated for accurate tracking of infarct size. We chose to use edema correction according to a reproducible method used to estimate brain swelling in rodents[88]. Although large lesional swelling volume has been found to predict poor outcome in patients with hemispheric stroke, edema alone does not account for the deficits observed in our study[124]. However, edema progression greatly masked LV and hindered the accurate estimation of stroke size in our model.

We also noticed a discrepancy between infarct size and neurological deficit in the mouse MCAO model, therefore we examined this paradoxical relationship more in detail. Our study provides evidence that infarct size measured alone is not a consistent indicator of sensorimotor deficits in acute ischemic stroke. In addition to some clinical reports, we have demonstrated here that there are unpredictable individual cases in the mouse MCAO model in which the expected trends do not prevail and infarct size does not show a correlation with the neurological outcome. The data presented here demonstrate that relying on lesion volume alone to predict AIS outcome may lead to an incorrect prognosis. In our experimental groups, one-fifth of the animals (3/15 mice) showed an "atypical prognosis" (mild lesion volume associated with severe neurological deficit). Exclusion or outlier filtering of these cases from experimental studies leads to incorrect conclusions because the data are overly optimized for homogeneity, do not represent variations in real populations, and thus do not translate to the clinical cases. Such irreproducible experimental AIS results have misled the field and contributed to the translational gap[26].

Stroke research is saturated with over 1000 successful preclinical pharmacological treatment studies that have failed to translate into routine clinical care[26]. The reason for the continuous failure remains unclear, but several factors are suspected. For instance, in animal AIS models, the follow-up period is much shorter than in the clinic (typically between 1week and 1month), and there is no universal, widely accepted symptom scale, so lesion volume is taken as a standardized measure of outcome[125]. Predicting functional outcome in rodents is as complicated and multifactorial as it is in humans. Furthermore, the intention to create standardized and uniform experimental groups for better statistical comparison may obscure the natural diversity of stroke presentation, which is found in humans[126].

The variability of infarct size in rodent MCAO models complicates and biases the desired homogeneity of subjects[26]. Although robust earlier studies demonstrated significant correlations between infarct volumes and neurological outcomes in mice and rats[98], the predictive value of early infarct assessment, such as neuroimaging at 24 hours, has been shown to depend on the timing of MRI and the duration of MCAO[127]. A more recent study confirms that lesion topology may increase predictive accuracy when using neuroimaging to characterize residual deficit in mice[127]. Importantly, the same study suggests that a subset of anatomical structures within the infarct area may be particularly influential in predicting long-term stroke outcome. Taking this into account, 2 of the possible explanations for the atypical prognosis in our study, among many others, could be (i) the localization of the infarct[128, 129], whose inclusion in the prediction model could also improve the estimation of residual deficit[127] or (ii) the clinical-DWI mismatch

phenomenon known from clinical studies[130-132]. The clinical-DWI mismatch describes that severe acute clinical symptoms may be accompanied by mild visible LV on DWI images, which compromises the evaluation or prediction of early AIS outcome and final lesion size[133]. In the subacute phase, discrepancy between imaging results and neurological status may signal lesion evolution by a secondary pathological mechanism. Also, clinically observed severe symptoms inconsistent with small LV may result from dynamic collateral recruitment of distant brain regions[134]. Consistent with this, AIS patients with perfusion deficits have higher NIHSS scores[134, 135]. Taken together, the paradoxical relationship of sensorimotor deficit and lesion volume after AIS is also detectable in clinical settings, and this paradox may be resolved by careful assessment of cortical involvement.

NOVEL OBSERVATIONS

The main novel observations of this study are as follows:

1. We demonstrated that spreading depolarization induces an **elevation of intracellular Ca^{2+} levels** in cortical astrocytes, capable of activating Ca^{2+} dependent intracellular pathways. Moreover, this is the first in vivo study to describe the **delayed astrocytic Ca^{2+} oscillations** following SD.
2. Although previous studies have reported an edema-limiting effect of the calmodulin inhibitor **trifluoperazine (TFP)**, our results **showed no influence** of the compound **on brain swelling following acute ischemic insult** in a mouse model. However, **TFP treatment reduced ischemic lesion volume and improved functional outcomes** 72 hours after the insult. We propose that its mechanism of action involves **improved neurovascular coupling and increased cerebral blood flow**.
3. Our findings highlight the **lack of correlation between ischemic lesion volume and the observable neurological deficit** in mice 72 hours after transient middle cerebral artery occlusion. Excluding atypical cases with small lesion volumes but severe functional deficits strengthened the correlation, although it still did not reach statistical significance. We suspect that lesion localization plays a key role.

SUMMARY

This work investigated whether early modulation of cytotoxic edema can mitigate secondary tissue damage after acute ischemic stroke (AIS) by targeting the Ca^{2+}-dependent intracellular trafficking of aquaporin-4 (AQP4). We focused on the hyperacute phase, when astrocyte swelling and ionic imbalance critically influence lesion maturation and long-term neurological outcome.

First, we characterized astrocytic Ca^{2+} responses to spreading depolarizations (SDs), key drivers of cytotoxic edema and metabolic failure after AIS. Using in vivo two-photon imaging cerebro-cortical astrocytes, we identified fast-propagating Ca^{2+} waves followed by delayed, low-frequency oscillations—an in vivo pattern not previously reported. These Ca^{2+} dynamics, partly mediated by TRPV4 channels, are hypothesized to provide a potent stimulus for calmodulin-dependent AQP4 translocation, linking SD-evoked Ca^{2+} influx to increased astrocyte water permeability during early injury. Building on this putative mechanism, we evaluated the effect of trifluoperazine (TFP), a calmodulin inhibitor that transiently blocks AQP4 trafficking while preserving its physiological roles on early AIS outcome. Administered after recanalization in a mouse MCAO model, TFP did not reduce edema volume on MRI at day three, yet significantly decreased infarct size and improved neurological performance, especially when given immediately after reperfusion. This dissociation suggests that early cytotoxic edema and infarct maturation can be attenuated independently of later vasogenic edema, which likely dominated MRI findings at the chosen time point. SPECT assessments confirmed that blood–brain barrier permeability remained unchanged, and supporting experiments in acute brain slices showed that TFP reduces rapid tissue swelling and AQP4 membrane accumulation, while in vivo assessments confirmed that blood–brain barrier permeability remained unchanged.

A critical additional observation made during this work concerns the paradoxical relationship between infarct size and neurological deficit. We observed that lesion volume alone is an unreliable predictor of functional outcome: nearly one-fifth of our MCAO mice displayed an “atypical prognosis,” exhibiting small infarcts but severe sensorimotor deficits. Excluding such cases—as is common practice—creates artificially homogeneous datasets that fail to reflect biological variability and undermine translational validity. This issue mirrors clinical observations, where lesion volume often fails to predict early severity or long-term outcome, and where factors such as lesion topology, cortical involvement, collateral recruitment, and

clinical–DWI mismatch critically influence presentation and recovery. Our findings thus reinforce that functional outcome in AIS depends on complex neuroanatomical and vascular factors, not lesion size alone, and that embracing—not filtering—variability is essential for reproducible and clinically relevant preclinical research.

Taken together, our work demonstrates that selectively modulating AQP4 trafficking during a narrow hyperacute window can attenuate early injury processes without impairing later edema resolution. Owing to its compatibility with reperfusion therapy and its established clinical approval, TFP represents a promising candidate for repurposing to mitigate early secondary injury following AIS. More broadly, our findings highlight the necessity of integrating functional, anatomical, and mechanistic endpoints to overcome long-standing translational barriers in stroke research.

ACKNOWLEDGEMENTS

I consider myself a lucky person indeed, as I've always had the chance to work in fields that genuinely interest me and have always been fond of my job. As a result — as the saying goes — I feel as though I haven't really had to work a single day in my life so far. This would not have been possible without some truly exceptional people.

Firstly, I would like to express my sincere gratitude to my group leader and the Head of the Department of Cell Biology and Molecular Medicine, Prof. Dr. Eszter Farkas. Eszter believed in me from my first day on, when I joined the group as a first year medical student. Thank you, for supporting me in pursuing all my goals, my good and even my less good ideas.

I am beyond grateful to my supervisor, Dr. Ákos Menyhárt. His enthusiasm, his ideas and his motivation always made him a role model and inspired me. Thank you for always creating a motivating, cheerful environment filled not only with great science but also humor, and for being there for me not only as a supervisor, but also as a friend in times when I needed one.

Special thanks to Prof. Dr. Ferenc Bari for supporting our group, our work, our scientific advancement.

I am deeply grateful to my lab members, especially Dr. Anna Törteli, for sharing this PhD journey with me and for becoming a true friend, and to Dr. Rita Frank for always being a kind and protective presence for both of us.

I also thank my family for their unwavering love and support throughout these years.

I am grateful to my friends who stood by me from the very beginning of my scientific journey, as well as to those I met along the way – you guys are pure joy and I am the luckiest to have you. Thank you for always patiently listening to my endless gushing about astrocytes.

And last but not least, I would like to thank You, the reader, for the opportunity to share my work with You.

REFERENCES

1. Feigin VL, Brainin M, Norrving B, et al. World Stroke Organization: Global Stroke Fact Sheet 2025. *Int J Stroke* 2025; 20: 132-144. 20250103. DOI: 10.1177/17474930241308142.
2. Hilkens NA, Casolla B, Leung TW, et al. Stroke. *Lancet* 2024; 403: 2820-2836. 2024/05/18. DOI: 10.1016/S0140-6736(24)00642-1.
3. Campbell BCV, De Silva DA, Macleod MR, et al. Ischaemic stroke. *Nat Rev Dis Primers* 2019; 5: 70. 2019/10/12. DOI: 10.1038/s41572-019-0118-8.
4. Martin SS, Aday AW, Almarzooq ZI, et al. 2024 Heart Disease and Stroke Statistics: A Report of US and Global Data From the American Heart Association. *Circulation* 2024; 149: e347-e913. 2024/01/24. DOI: 10.1161/CIR.0000000000001209.
5. Magid-Bernstein J, Girard R, Polster S, et al. Cerebral Hemorrhage: Pathophysiology, Treatment, and Future Directions. *Circ Res* 2022; 130: 1204-1229. 2022/04/15. DOI: 10.1161/CIRCRESAHA.121.319949.
6. Ikawa F, Michihata N, Matsushige T, et al. In-hospital mortality and poor outcome after surgical clipping and endovascular coiling for aneurysmal subarachnoid hemorrhage using nationwide databases: a systematic review and meta-analysis. *Neurosurg Rev* 2020; 43: 655-667. 2019/04/04. DOI: 10.1007/s10143-019-01096-2.
7. Hoh BL, Ko NU, Amin-Hanjani S, et al. 2023 Guideline for the Management of Patients With Aneurysmal Subarachnoid Hemorrhage: A Guideline From the American Heart Association/American Stroke Association. *Stroke* 2023; 54: e314-e370. 2023/05/22. DOI: 10.1161/STR.0000000000000436.
8. Adams HP, Jr., Bendixen BH, Kappelle LJ, et al. Classification of subtype of acute ischemic stroke. Definitions for use in a multicenter clinical trial. TOAST. Trial of Org 10172 in Acute Stroke Treatment. *Stroke* 1993; 24: 35-41. 1993/01/01. DOI: 10.1161/01.str.24.1.35.
9. Amarenco P, Bogousslavsky J, Caplan LR, et al. New approach to stroke subtyping: the A-S-C-O (phenotypic) classification of stroke. *Cerebrovasc Dis* 2009; 27: 502-508. 2009/04/04. DOI: 10.1159/000210433.
10. Arsava EM, Ballabio E, Benner T, et al. The Causative Classification of Stroke system: an international reliability and optimization study. *Neurology* 2010; 75: 1277-1284. 2010/10/06. DOI: 10.1212/WNL.0b013e3181f612ce.
11. Rennert RC, Wali AR, Steinberg JA, et al. Epidemiology, Natural History, and Clinical Presentation of Large Vessel Ischemic Stroke. *Neurosurgery* 2019; 85: S4-S8. 2019/06/15. DOI: 10.1093/neuros/nyz042.
12. Astrup J, Siesjo BK and Symon L. Thresholds in cerebral ischemia - the ischemic penumbra. *Stroke* 1981; 12: 723-725. 1981/11/01. DOI: 10.1161/01.str.12.6.723.
13. Baron JC. Protecting the ischaemic penumbra as an adjunct to thrombectomy for acute stroke. *Nat Rev Neurol* 2018; 14: 325-337. 2018/04/21. DOI: 10.1038/s41582-018-0002-2.
14. Prabhakaran S, Gonzalez NR, Zachrison KS, et al. 2026 Guideline for the Early Management of Patients With Acute Ischemic Stroke: A Guideline From the American Heart Association/American Stroke Association. *Stroke* 2026 2026/01/26. DOI: 10.1161/STR.0000000000000513.
15. Gauberti M, De Lizarrondo SM and Vivien D. The "inflammatory penumbra" in ischemic stroke: From clinical data to experimental evidence. *Eur Stroke J* 2016; 1: 20-27. 2016/03/01. DOI: 10.1177/2396987316630249.
16. Ma H, Campbell BCV, Parsons MW, et al. Thrombolysis Guided by Perfusion Imaging up to 9 Hours after Onset of Stroke. *N Engl J Med* 2019; 380: 1795-1803. 2019/05/09. DOI: 10.1056/NEJMoa1813046.
17. Menon BK, Buck BH, Singh N, et al. Intravenous tenecteplase compared with alteplase for acute ischaemic stroke in Canada (AcT): a pragmatic, multicentre, open-label, registry-linked, randomised, controlled, non-inferiority trial. *Lancet* 2022; 400: 161-169. 2022/07/03. DOI: 10.1016/S0140-6736(22)01054-6.

18. Nogueira RG, Jadhav AP, Haussen DC, et al. Thrombectomy 6 to 24 Hours after Stroke with a Mismatch between Deficit and Infarct. *N Engl J Med* 2018; 378: 11-21. 2017/11/14. DOI: 10.1056/NEJMoa1706442.
19. Albers GW, Marks MP, Kemp S, et al. Thrombectomy for Stroke at 6 to 16 Hours with Selection by Perfusion Imaging. *N Engl J Med* 2018; 378: 708-718. 2018/01/25. DOI: 10.1056/NEJMoa1713973.
20. Bendszus M, Fiehler J, Subtil F, et al. Endovascular thrombectomy for acute ischaemic stroke with established large infarct: multicentre, open-label, randomised trial. *Lancet* 2023; 402: 1753-1763. 2023/10/15. DOI: 10.1016/S0140-6736(23)02032-9.
21. Huo X, Ma G, Tong X, et al. Trial of Endovascular Therapy for Acute Ischemic Stroke with Large Infarct. *N Engl J Med* 2023; 388: 1272-1283. 2023/02/11. DOI: 10.1056/NEJMoa2213379.
22. Sarraj A, Hassan AE, Abraham MG, et al. Trial of Endovascular Thrombectomy for Large Ischemic Strokes. *N Engl J Med* 2023; 388: 1259-1271. 2023/02/11. DOI: 10.1056/NEJMoa2214403.
23. Hernandez-Perez M, Werner M, Remollo S, et al. Early and Delayed Infarct Growth in Patients Undergoing Mechanical Thrombectomy: A Prospective, Serial MRI Study. *Stroke* 2023; 54: 217-225. 2022/11/04. DOI: 10.1161/STROKEAHA.122.039090.
24. Bai J and Lyden PD. Revisiting cerebral postischemic reperfusion injury: new insights in understanding reperfusion failure, hemorrhage, and edema. *Int J Stroke* 2015; 10: 143-152. 2015/01/20. DOI: 10.1111/ijs.12434.
25. Butler D. Translational research: crossing the valley of death. *Nature* 2008; 453: 840-842. DOI: 10.1038/453840a.
26. Lourbopoulos A, Mourouzis I, Xinaris C, et al. Translational Block in Stroke: A Constructive and "Out-of-the-Box" Reappraisal. *Front Neurosci* 2021; 15: 652403. 2021/06/01. DOI: 10.3389/fnins.2021.652403.
27. Bala F, Ospel J, Mulpur B, et al. Infarct Growth despite Successful Endovascular Reperfusion in Acute Ischemic Stroke: A Meta-analysis. *AJNR Am J Neuroradiol* 2021; 42: 1472-1478. 2021/06/05. DOI: 10.3174/ajnr.A7177.
28. Miteff F, Levi CR, Bateman GA, et al. The independent predictive utility of computed tomography angiographic collateral status in acute ischaemic stroke. *Brain* 2009; 132: 2231-2238. 2009/06/11. DOI: 10.1093/brain/awp155.
29. Menyhart A, Frank R, Farkas AE, et al. Malignant astrocyte swelling and impaired glutamate clearance drive the expansion of injurious spreading depolarization foci. *J Cereb Blood Flow Metab* 2022; 42: 584-599. 2021/08/25. DOI: 10.1177/0271678X211040056.
30. Torteli A, Toth R, Bari F, et al. Collateral is brain: Low perfusion triggers spreading depolarization and futile reperfusion after acute ischemic stroke. *J Cereb Blood Flow Metab* 2024; 44: 1881-1887. 2024/09/03. DOI: 10.1177/0271678X241270480.
31. Dreier JP and Reiffurth C. The stroke-migraine depolarization continuum. *Neuron* 2015; 86: 902-922. 2015/05/23. DOI: 10.1016/j.neuron.2015.04.004.
32. Dreier JP. The role of spreading depression, spreading depolarization and spreading ischemia in neurological disease. *Nat Med* 2011; 17: 439-447. 2011/04/09. DOI: 10.1038/nm.2333.
33. Leao AAP. SPREADING DEPRESSION OF ACTIVITY IN THE CEREBRAL CORTEX. 1944; 7: 359-390. DOI: 10.1152/jn.1944.7.6.359.
34. Hartings JA, Shuttleworth CW, Kirov SA, et al. The continuum of spreading depolarizations in acute cortical lesion development: Examining Leao's legacy. *J Cereb Blood Flow Metab* 2017; 37: 1571-1594. 2016/06/23. DOI: 10.1177/0271678X16654495.
35. Farkas E, Bari F and Obrenovitch TP. Multi-modal imaging of anoxic depolarization and hemodynamic changes induced by cardiac arrest in the rat cerebral cortex. *Neuroimage* 2010; 51: 734-742. 2010/03/02. DOI: 10.1016/j.neuroimage.2010.02.055.
36. Hinzman JM, Andaluz N, Shutter LA, et al. Inverse neurovascular coupling to cortical spreading depolarizations in severe brain trauma. *Brain* 2014; 137: 2960-2972. 2014/08/27. DOI: 10.1093/brain/awu241.

37. Dreier JP, Major S, Foreman B, et al. Terminal spreading depolarization and electrical silence in death of human cerebral cortex. *Ann Neurol* 2018; 83: 295-310. 2018/01/14. DOI: 10.1002/ana.25147.
38. Dreier JP, Fabricius M, Ayata C, et al. Recording, analysis, and interpretation of spreading depolarizations in neurointensive care: Review and recommendations of the COSBID research group. *J Cereb Blood Flow Metab* 2017; 37: 1595-1625. 2016/06/19. DOI: 10.1177/0271678X16654496.
39. Ayata C and Lauritzen M. Spreading Depression, Spreading Depolarizations, and the Cerebral Vasculature. *Physiol Rev* 2015; 95: 953-993. 2015/07/03. DOI: 10.1152/physrev.00027.2014.
40. Hoffmann U and Ayata C. Neurovascular coupling during spreading depolarizations. *Acta Neurochir Suppl* 2013; 115: 161-165. 2012/08/15. DOI: 10.1007/978-3-7091-1192-5_31.
41. Bere Z, Obrenovitch TP, Kozak G, et al. Imaging reveals the focal area of spreading depolarizations and a variety of hemodynamic responses in a rat microembolic stroke model. *J Cereb Blood Flow Metab* 2014; 34: 1695-1705. 2014/07/31. DOI: 10.1038/jcbfm.2014.136.
42. Major S, Petzold GC, Reiffurth C, et al. A role of the sodium pump in spreading ischemia in rats. *J Cereb Blood Flow Metab* 2017; 37: 1687-1705. 2016/03/20. DOI: 10.1177/0271678X16639059.
43. Dreier JP, Lemale CL, Kola V, et al. Spreading depolarization is not an epiphenomenon but the principal mechanism of the cytotoxic edema in various gray matter structures of the brain during stroke. *Neuropharmacology* 2018; 134: 189-207. 2017/09/25. DOI: 10.1016/j.neuropharm.2017.09.027.
44. Simard JM, Kent TA, Chen M, et al. Brain oedema in focal ischaemia: molecular pathophysiology and theoretical implications. *Lancet Neurol* 2007; 6: 258-268. 2007/02/17. DOI: 10.1016/S1474-4422(07)70055-8.
45. Mestre H, Du T, Sweeney AM, et al. Cerebrospinal fluid influx drives acute ischemic tissue swelling. *Science* 2020; 367 2020/02/01. DOI: 10.1126/science.aax7171.
46. Bardutzky J and Schwab S. Antiedema therapy in ischemic stroke. *Stroke* 2007; 38: 3084-3094. 2007/09/29. DOI: 10.1161/STROKEAHA.107.490193.
47. Ng FC, Yassi N, Sharma G, et al. Cerebral Edema in Patients With Large Hemispheric Infarct Undergoing Reperfusion Treatment: A HERMES Meta-Analysis. *Stroke* 2021; 52: 3450-3458. 2021/08/14. DOI: 10.1161/STROKEAHA.120.033246.
48. Cook AM, Morgan Jones G, Hawryluk GWJ, et al. Guidelines for the Acute Treatment of Cerebral Edema in Neurocritical Care Patients. *Neurocrit Care* 2020; 32: 647-666. 2020/04/01. DOI: 10.1007/s12028-020-00959-7.
49. Berge E, Whiteley W, Audebert H, et al. European Stroke Organisation (ESO) guidelines on intravenous thrombolysis for acute ischaemic stroke. *Eur Stroke J* 2021; 6: I-LXII. 2021/04/06. DOI: 10.1177/2396987321989865.
50. Simard JM, Wilhelmy B, Tsymbalyuk N, et al. Brain Swelling versus Infarct Size: A Problematizing Review. *Brain Sci* 2024; 14 2024/03/28. DOI: 10.3390/brainsci14030229.
51. Stokum JA, Gerzanich V and Simard JM. Molecular pathophysiology of cerebral edema. *J Cereb Blood Flow Metab* 2016; 36: 513-538. 2015/12/15. DOI: 10.1177/0271678X15617172.
52. Klatzo I. Pathophysiological aspects of brain edema. *Acta Neuropathol* 1987; 72: 236-239. 1987/01/01. DOI: 10.1007/BF00691095.
53. Thrane AS, Rangroo Thrane V and Nedergaard M. Drowning stars: reassessing the role of astrocytes in brain edema. *Trends Neurosci* 2014; 37: 620-628. 2014/09/23. DOI: 10.1016/j.tins.2014.08.010.
54. Iliff JJ, Wang M, Liao Y, et al. A paravascular pathway facilitates CSF flow through the brain parenchyma and the clearance of interstitial solutes, including amyloid beta. *Sci Transl Med* 2012; 4: 147ra111. 2012/08/17. DOI: 10.1126/scitranslmed.3003748.
55. Jessen NA, Munk AS, Lundgaard I, et al. The Glymphatic System: A Beginner's Guide. *Neurochem Res* 2015; 40: 2583-2599. 2015/05/08. DOI: 10.1007/s11064-015-1581-6.
56. Liebeskind DS, Juttler E, Shapovalov Y, et al. Cerebral Edema Associated With Large Hemispheric Infarction. *Stroke* 2019; 50: 2619-2625. 2019/08/21. DOI: 10.1161/STROKEAHA.118.024766.

57. Ribeiro Mde C, Hirt L, Bogousslavsky J, et al. Time course of aquaporin expression after transient focal cerebral ischemia in mice. *J Neurosci Res* 2006; 83: 1231-1240. 2006/03/03. DOI: 10.1002/jnr.20819.
58. Garcia Rios CA and Leon-Rojas JE. Aquaporin-4 in Stroke and Brain Edema-Friend or Foe? *Int J Mol Sci* 2025; 26 2025/09/13. DOI: 10.3390/ijms26178178.
59. Iadecola C and Nedergaard M. Glial regulation of the cerebral microvasculature. *Nat Neurosci* 2007; 10: 1369-1376. 2007/10/30. DOI: 10.1038/nn2003.
60. Bojovic D, Dagostin A, Sullivan SJ, et al. Astrocyte gap junctions and K (ir) channels contribute to K(+) buffering and regulate neuronal excitability. *Front Cell Neurosci* 2025; 19: 1571218. 2025/12/08. DOI: 10.3389/fncel.2025.1571218.
61. Nagelhus EA, Mathiisen TM and Ottersen OP. Aquaporin-4 in the central nervous system: cellular and subcellular distribution and coexpression with KIR4.1. *Neuroscience* 2004; 129: 905-913. 2004/11/25. DOI: 10.1016/j.neuroscience.2004.08.053.
62. Nagelhus EA and Ottersen OP. Physiological roles of aquaporin-4 in brain. *Physiol Rev* 2013; 93: 1543-1562. 2013/10/19. DOI: 10.1152/physrev.00011.2013.
63. Manley GT, Fujimura M, Ma T, et al. Aquaporin-4 deletion in mice reduces brain edema after acute water intoxication and ischemic stroke. *Nat Med* 2000; 6: 159-163. 2000/02/02. DOI: 10.1038/72256.
64. Hirt L, Ternon B, Price M, et al. Protective role of early aquaporin 4 induction against postischemic edema formation. *J Cereb Blood Flow Metab* 2009; 29: 423-433. 2008/11/06. DOI: 10.1038/jcbfm.2008.133.
65. Badaut J, Fukuda AM, Jullienne A, et al. Aquaporin and brain diseases. *Biochim Biophys Acta* 2014; 1840: 1554-1565. 2014/02/12. DOI: 10.1016/j.bbagen.2013.10.032.
66. Stokum JA, Kwon MS, Woo SK, et al. SUR1-TRPM4 and AQP4 form a heteromultimeric complex that amplifies ion/water osmotic coupling and drives astrocyte swelling. *Glia* 2018; 66: 108-125. 2017/09/15. DOI: 10.1002/glia.23231.
67. Salman MM, Kitchen P, Halsey A, et al. Emerging roles for dynamic aquaporin-4 subcellular relocalization in CNS water homeostasis. *Brain* 2022; 145: 64-75. 2021/09/10. DOI: 10.1093/brain/awab311.
68. Verkman AS, Binder DK, Bloch O, et al. Three distinct roles of aquaporin-4 in brain function revealed by knockout mice. *Biochim Biophys Acta* 2006; 1758: 1085-1093. 2006/03/28. DOI: 10.1016/j.bbamem.2006.02.018.
69. Papadopoulos MC and Verkman AS. Aquaporin-4 and brain edema. *Pediatr Nephrol* 2007; 22: 778-784. 2007/03/10. DOI: 10.1007/s00467-006-0411-0.
70. Hirt L, Fukuda AM, Ambadipudi K, et al. Improved long-term outcome after transient cerebral ischemia in aquaporin-4 knockout mice. *J Cereb Blood Flow Metab* 2017; 37: 277-290. 2016/01/16. DOI: 10.1177/0271678X15623290.
71. Kitchen P, Day RE, Taylor LH, et al. Identification and Molecular Mechanisms of the Rapid Tonicity-induced Relocalization of the Aquaporin 4 Channel. *J Biol Chem* 2015; 290: 16873-16881. 2015/05/28. DOI: 10.1074/jbc.M115.646034.
72. Ren Z, Iliff JJ, Yang L, et al. 'Hit & Run' model of closed-skull traumatic brain injury (TBI) reveals complex patterns of post-traumatic AQP4 dysregulation. *J Cereb Blood Flow Metab* 2013; 33: 834-845. 2013/02/28. DOI: 10.1038/jcbfm.2013.30.
73. Steiner E, Enzmann GU, Lin S, et al. Loss of astrocyte polarization upon transient focal brain ischemia as a possible mechanism to counteract early edema formation. *Glia* 2012; 60: 1646-1659. 2012/07/12. DOI: 10.1002/glia.22383.
74. Amiry-Moghaddam M, Frydenlund DS and Ottersen OP. Anchoring of aquaporin-4 in brain: molecular mechanisms and implications for the physiology and pathophysiology of water transport. *Neuroscience* 2004; 129: 999-1010. 2004/11/25. DOI: 10.1016/j.neuroscience.2004.08.049.
75. Kitchen P, Salman MM, Halsey AM, et al. Targeting Aquaporin-4 Subcellular Localization to Treat Central Nervous System Edema. *Cell* 2020; 181: 784-799 e719. 2020/05/16. DOI: 10.1016/j.cell.2020.03.037.

76. Profeta GS, Dos Reis CV, Santiago ADS, et al. Binding and structural analyses of potent inhibitors of the human Ca(2+)/calmodulin dependent protein kinase kinase 2 (CAMKK2) identified from a collection of commercially-available kinase inhibitors. *Sci Rep* 2019; 9: 16452. 2019/11/13. DOI: 10.1038/s41598-019-52795-1.
77. Sylvain NJ, Salman MM, Pushie MJ, et al. The effects of trifluoperazine on brain edema, aquaporin-4 expression and metabolic markers during the acute phase of stroke using photothrombotic mouse model. *Biochim Biophys Acta Biomembr* 2021; 1863: 183573. 2021/02/10. DOI: 10.1016/j.bbamem.2021.183573.
78. Kilkenny C, Browne W, Cuthill IC, et al. Animal research: reporting in vivo experiments: the ARRIVE guidelines. *Br J Pharmacol* 2010; 160: 1577-1579. 2010/07/24. DOI: 10.1111/j.1476-5381.2010.00872.x.
79. Hulsmann S, Hagos L, Heuer H, et al. Limitations of Sulforhodamine 101 for Brain Imaging. *Front Cell Neurosci* 2017; 11: 44. 2017/03/16. DOI: 10.3389/fncel.2017.00044.
80. Tan SS, Kalloniatis M, Truong HT, et al. Oligodendrocyte positioning in cerebral cortex is independent of projection neuron layering. *Glia* 2009; 57: 1024-1030. 2008/12/09. DOI: 10.1002/glia.20826.
81. Menyhart A, Farkas AE, Varga DP, et al. Large-conductance Ca(2+)-activated potassium channels are potently involved in the inverse neurovascular response to spreading depolarization. *Neurobiol Dis* 2018; 119: 41-52. 2018/07/28. DOI: 10.1016/j.nbd.2018.07.026.
82. Koizumi J-i, Yoshida Y, Nakazawa T, et al. Experimental studies of ischemic brain edema

1. A new experimental model of cerebral embolism in rats in which recirculation can be introduced in the ischemic area. *Nosotchu* 1986; 8: 1-8. DOI: 10.3995/jstroke.8.1.
83. Lourbopoulos A, Mamrak U, Roth S, et al. Inadequate food and water intake determine mortality following stroke in mice. *J Cereb Blood Flow Metab* 2017; 37: 2084-2097. 2016/07/28. DOI: 10.1177/0271678X16660986.
84. Pinto R, Magalhaes A, Sousa M, et al. Bridging the Transient Intraluminal Stroke Preclinical Model to Clinical Practice: From Improved Surgical Procedures to a Workflow of Functional Tests. *Front Neurol* 2022; 13: 846735. 2022/04/02. DOI: 10.3389/fneur.2022.846735.
85. Krafft PR, McBride DW, Lekic T, et al. Correlation between subacute sensorimotor deficits and brain edema in two mouse models of intracerebral hemorrhage. *Behav Brain Res* 2014; 264: 151-160. 2014/02/13. DOI: 10.1016/j.bbr.2014.01.052.
86. Toth R, Farkas AE, Krizbai IA, et al. Astrocyte Ca(2+) Waves and Subsequent Non-Synchronized Ca(2+) Oscillations Coincide with Arteriole Diameter Changes in Response to Spreading Depolarization. *Int J Mol Sci* 2021; 22 2021/04/04. DOI: 10.3390/ijms22073442.
87. Toth R, Szabo N, Torteli A, et al. The paradoxical relationship of sensorimotor deficit and lesion volume in acute ischemic stroke. *J Neuropathol Exp Neurol* 2025; 84: 771-779. 2025/04/24. DOI: 10.1093/jnen/nlaf046.
88. Gerriets T, Stolz E, Walberer M, et al. Noninvasive quantification of brain edema and the space-occupying effect in rat stroke models using magnetic resonance imaging. *Stroke* 2004; 35: 566-571. 2004/01/24. DOI: 10.1161/01.STR.0000113692.38574.57.
89. Hotaling NA, Bharti K, Kriel H, et al. DiameterJ: A validated open source nanofiber diameter measurement tool. *Biomaterials* 2015; 61: 327-338. 2015/06/05. DOI: 10.1016/j.biomaterials.2015.05.015.
90. Fellin T, Pascual O, Gobbo S, et al. Neuronal synchrony mediated by astrocytic glutamate through activation of extrasynaptic NMDA receptors. *Neuron* 2004; 43: 729-743. 2004/09/02. DOI: 10.1016/j.neuron.2004.08.011.
91. Perea G and Araque A. Astrocytes potentiate transmitter release at single hippocampal synapses. *Science* 2007; 317: 1083-1086. 2007/08/25. DOI: 10.1126/science.1144640.
92. Chuquet J, Hollender L and Nimchinsky EA. High-resolution in vivo imaging of the neurovascular unit during spreading depression. *J Neurosci* 2007; 27: 4036-4044. 2007/04/13. DOI: 10.1523/JNEUROSCI.0721-07.2007.

93. Shvedova M, Islam MR, Armoundas AA, et al. Modified middle cerebral artery occlusion model provides detailed intraoperative cerebral blood flow registration and improves neurobehavioral evaluation. *J Neurosci Methods* 2021; 358: 109179. 2021/04/06. DOI: 10.1016/j.jneumeth.2021.109179.
94. Torteli A, Toth R, Berger S, et al. Spreading depolarization causes reperfusion failure after cerebral ischemia. *J Cereb Blood Flow Metab* 2023; 43: 655-664. 2023/01/28. DOI: 10.1177/0271678X231153745.
95. Schaefer PW, Pulli B, Copen WA, et al. Combining MRI with NIHSS thresholds to predict outcome in acute ischemic stroke: value for patient selection. *AJNR Am J Neuroradiol* 2015; 36: 259-264. 2014/09/27. DOI: 10.3174/ajnr.A4103.
96. Heldner MR, Zubler C, Mattle HP, et al. National Institutes of Health stroke scale score and vessel occlusion in 2152 patients with acute ischemic stroke. *Stroke* 2013; 44: 1153-1157. 2013/03/09. DOI: 10.1161/STROKEAHA.111.000604.
97. Thijs VN, Lansberg MG, Beaulieu C, et al. Is early ischemic lesion volume on diffusion-weighted imaging an independent predictor of stroke outcome? A multivariable analysis. *Stroke* 2000; 31: 2597-2602. 2000/11/04. DOI: 10.1161/01.str.31.11.2597.
98. Sutherland BA and Buchan AM. Alteplase treatment does not increase brain injury after mechanical middle cerebral artery occlusion in the rat. *J Cereb Blood Flow Metab* 2013; 33: e1-7. 2013/08/22. DOI: 10.1038/jcbfm.2013.148.
99. Hassinger TD, Guthrie PB, Atkinson PB, et al. An extracellular signaling component in propagation of astrocytic calcium waves. *Proc Natl Acad Sci U S A* 1996; 93: 13268-13273. 1996/11/12. DOI: 10.1073/pnas.93.23.13268.
100. Newman EA and Zahs KR. Calcium waves in retinal glial cells. *Science* 1997; 275: 844-847. 1997/02/07. DOI: 10.1126/science.275.5301.844.
101. Enger R, Tang W, Vindedal GF, et al. Dynamics of Ionic Shifts in Cortical Spreading Depression. *Cereb Cortex* 2015; 25: 4469-4476. 2015/04/04. DOI: 10.1093/cercor/bhv054.
102. Wu DC, Chen RY, Cheng TC, et al. Spreading Depression Promotes Astrocytic Calcium Oscillations and Enhances Gliotransmission to Hippocampal Neurons. *Cereb Cortex* 2018; 28: 3204-3216. 2017/10/06. DOI: 10.1093/cercor/bhx192.
103. Peters O, Schipke CG, Hashimoto Y, et al. Different mechanisms promote astrocyte Ca2+ waves and spreading depression in the mouse neocortex. *J Neurosci* 2003; 23: 9888-9896. 2003/10/31. DOI: 10.1523/JNEUROSCI.23-30-09888.2003.
104. Parri HR, Gould TM and Crunelli V. Spontaneous astrocytic Ca2+ oscillations in situ drive NMDAR-mediated neuronal excitation. *Nat Neurosci* 2001; 4: 803-812. 2001/07/31. DOI: 10.1038/90507.
105. Dunn KM, Hill-Eubanks DC, Liedtke WB, et al. TRPV4 channels stimulate Ca2+-induced Ca2+ release in astrocytic endfeet and amplify neurovascular coupling responses. *Proc Natl Acad Sci U S A* 2013; 110: 6157-6162. 2013/03/27. DOI: 10.1073/pnas.1216514110.
106. Rakers C, Schmid M and Petzold GC. TRPV4 channels contribute to calcium transients in astrocytes and neurons during peri-infarct depolarizations in a stroke model. *Glia* 2017; 65: 1550-1561. 2017/06/24. DOI: 10.1002/glia.23183.
107. Sucha P, Hermanova Z, Chmelova M, et al. The absence of AQP4/TRPV4 complex substantially reduces acute cytotoxic edema following ischemic injury. *Front Cell Neurosci* 2022; 16: 1054919. 2022/12/27. DOI: 10.3389/fncel.2022.1054919.
108. Hermanova Z, Valihrach L, Kriska J, et al. The deletion of AQP4 and TRPV4 affects astrocyte swelling/volume recovery in response to ischemia-mimicking pathologies. *Front Cell Neurosci* 2024; 18: 1393751. 2024/05/31. DOI: 10.3389/fncel.2024.1393751.
109. Igarashi H, Huber VJ, Tsujita M, et al. Pretreatment with a novel aquaporin 4 inhibitor, TGN-020, significantly reduces ischemic cerebral edema. *Neurol Sci* 2011; 32: 113-116. 2010/10/07. DOI: 10.1007/s10072-010-0431-1.

110. Sun C, Lin L, Yin L, et al. Acutely Inhibiting AQP4 With TGN-020 Improves Functional Outcome by Attenuating Edema and Peri-Infarct Astrogliosis After Cerebral Ischemia. *Front Immunol* 2022; 13: 870029. 2022/05/21. DOI: 10.3389/fimmu.2022.870029.
111. Zhang W, Chen S, Ma B, et al. Trifluoperazine regulates blood-brain barrier permeability via the MLCK/p-MLC pathway to promote ischemic stroke recovery. *iScience* 2024; 27: 109156. 2024/03/05. DOI: 10.1016/j.isci.2024.109156.
112. Igarashi H, Tsujita M, Suzuki Y, et al. Inhibition of aquaporin-4 significantly increases regional cerebral blood flow. *Neuroreport* 2013; 24: 324-328. 2013/03/07. DOI: 10.1097/WNR.0b013e32835fc827.
113. Attwell D, Buchan AM, Charpak S, et al. Glial and neuronal control of brain blood flow. *Nature* 2010; 468: 232-243. 2010/11/12. DOI: 10.1038/nature09613.
114. Seidel JL, Escartin C, Ayata C, et al. Multifaceted roles for astrocytes in spreading depolarization: A target for limiting spreading depolarization in acute brain injury? *Glia* 2016; 64: 5-20. 2015/08/25. DOI: 10.1002/glia.22824.
115. Risher WC, Croom D and Kirov SA. Persistent astroglial swelling accompanies rapid reversible dendritic injury during stroke-induced spreading depolarizations. *Glia* 2012; 60: 1709-1720. 2012/07/24. DOI: 10.1002/glia.22390.
116. Ostergaard L, Engedal TS, Aamand R, et al. Capillary transit time heterogeneity and flow-metabolism coupling after traumatic brain injury. *J Cereb Blood Flow Metab* 2014; 34: 1585-1598. 2014/07/24. DOI: 10.1038/jcbfm.2014.131.
117. Fordsmann JC, Ko RW, Choi HB, et al. Increased 20-HETE synthesis explains reduced cerebral blood flow but not impaired neurovascular coupling after cortical spreading depression in rat cerebral cortex. *J Neurosci* 2013; 33: 2562-2570. 2013/02/09. DOI: 10.1523/JNEUROSCI.2308-12.2013.
118. Li Z, McConnell HL, Stackhouse TL, et al. Increased 20-HETE Signaling Suppresses Capillary Neurovascular Coupling After Ischemic Stroke in Regions Beyond the Infarct. *Front Cell Neurosci* 2021; 15: 762843. 2021/11/26. DOI: 10.3389/fncel.2021.762843.
119. Mishra A, Gordon GR, MacVicar BA, et al. Astrocyte Regulation of Cerebral Blood Flow in Health and Disease. *Cold Spring Harb Perspect Biol* 2024; 16 2024/02/06. DOI: 10.1101/cshperspect.a041354.
120. Zhao W, Wu C, Dornbos D, 3rd, et al. Multiphase adjuvant neuroprotection: A novel paradigm for improving acute ischemic stroke outcomes. *Brain Circ* 2020; 6: 11-18. 2020/03/14. DOI: 10.4103/bc.bc_58_19.
121. Hacke W, Schwab S, Horn M, et al. 'Malignant' middle cerebral artery territory infarction: clinical course and prognostic signs. *Arch Neurol* 1996; 53: 309-315. 1996/04/01. DOI: 10.1001/archneur.1996.00550040037012.
122. Treadwell SD and Thanvi B. Malignant middle cerebral artery (MCA) infarction: pathophysiology, diagnosis and management. *Postgrad Med J* 2010; 86: 235-242. 2010/04/01. DOI: 10.1136/pgmj.2009.094292.
123. Koch S, Mueller S, Foddis M, et al. Atlas registration for edema-corrected MRI lesion volume in mouse stroke models. *J Cereb Blood Flow Metab* 2019; 39: 313-323. 2017/08/23. DOI: 10.1177/0271678X17726635.
124. Ostwaldt AC, Battey TWK, Irvine HJ, et al. Comparative Analysis of Markers of Mass Effect after Ischemic Stroke. *J Neuroimaging* 2018; 28: 530-534. 2018/05/26. DOI: 10.1111/jon.12525.
125. Lyden PD, Bosetti F, Diniz MA, et al. The Stroke Preclinical Assessment Network: Rationale, Design, Feasibility, and Stage 1 Results. *Stroke* 2022; 53: 1802-1812. 20220331. DOI: 10.1161/STROKEAHA.121.038047.
126. Prosser J, Butcher K, Allport L, et al. Clinical-diffusion mismatch predicts the putative penumbra with high specificity. *Stroke* 2005; 36: 1700-1704. 2005/07/16. DOI: 10.1161/01.STR.0000173407.40773.17.
127. Knab F, Koch SP, Major S, et al. Prediction of Stroke Outcome in Mice Based on Noninvasive MRI and Behavioral Testing. *Stroke* 2023; 54: 2895-2905. 2023/09/25. DOI: 10.1161/STROKEAHA.123.043897.

128. Alexander LD, Black SE, Gao F, et al. Correlating lesion size and location to deficits after ischemic stroke: the influence of accounting for altered peri-necrotic tissue and incidental silent infarcts. *Behav Brain Funct* 2010; 6: 6. 2010/03/09. DOI: 10.1186/1744-9081-6-6.
129. Konigsberg A, DeMarco AT, Mayer C, et al. Influence of stroke infarct location on quality of life assessed in a multivariate lesion-symptom mapping study. *Sci Rep* 2021; 11: 13490. 2021/07/01. DOI: 10.1038/s41598-021-92865-x.
130. Christian N, Ghanaati H, Changizi V, et al. Reliability of Clinical DWI Mismatch Approach to Predict Patient With the Probability of Large Infarct Growth: A Comparison of the Percentage of Infarct Growth and Clinical DWI Mismatch Status of the Patients With Acute Ischemic Stroke. 2020; 3: 92-99. DOI: 10.1177/2516608520959541.
131. Deng PP, Wu N, Chen XJ, et al. NIHSS-the Alberta Stroke Program Early CT Score mismatch in guiding thrombolysis in patients with acute ischemic stroke. *J Neurol* 2022; 269: 1515-1521. 2021/07/29. DOI: 10.1007/s00415-021-10704-5.
132. Dávalos A, Blanco M, Pedraza S, et al. The clinical–DWI mismatch. 2004; 62: 2187-2192. DOI: doi:10.1212/01.WNL.0000130570.41127.EA.
133. Malikova H, Kremenova K, Lukavsky J, et al. Early and late infarct growth rate in ischemic stroke patients after successful endovascular treatment in early time window: correlation of imaging and clinical factors with clinical outcome. *Quant Imaging Med Surg* 2023; 13: 5770-5782. 2023/09/15. DOI: 10.21037/qims-23-153.
134. Aswendt M, Pallast N, Wieters F, et al. Lesion Size- and Location-Dependent Recruitment of Contralesional Thalamus and Motor Cortex Facilitates Recovery after Stroke in Mice. *Transl Stroke Res* 2021; 12: 87-97. 2020/03/14. DOI: 10.1007/s12975-020-00802-3.
135. Filosa JA, Morrison HW, Iddings JA, et al. Beyond neurovascular coupling, role of astrocytes in the regulation of vascular tone. *Neuroscience* 2016; 323: 96-109. 2015/04/07. DOI: 10.1016/j.neuroscience.2015.03.064.